Modern Eddington Experiment 2024: Results and Conclusions

William A. Dittrich,[a] Don Bruns,[b] Richard Berry,[c] Kenneth Carrell,[d] Douglas Smith,[e] Andrew Smith,[f] Daniel Borrero-Echeverry,[g] Greg Mulder,[h] Heather Hill,[h] Greg Kinne,[i] Joseph M. Izen,[j] J. Jedediah Rembold,[k] Cesar Delgado,[l] Anna E. Hornbeck,[g] Sam A. Jeffe,[g] Jared R. McSorley,[g] Olivia E. Schutz,[k] Maddie Strate,[g] Ehsan Matin,[a] Jesse Kinder,[m] Paul Poncy,[n] Cade Freels,[n] Josue Benitez-Flores,[h] Rose Smith,[h] Bryan Bauer,[h] Calvin Rajendram,[h] Sara Leathers,[h] Luana Fenstermacher,[h] Michael Philip Clark,[h] Eve Kempe,[h] Tyler Slaght,[h] Kaleah Webb,[h] Colin Bradley,[h] Sophia Plascencia,[h] Gavin Le,[h] Austyn C. Moon,[h] Yoojin Choi,[d] Andrew Tom,[d] Stasha Youngquist,[d] Kelsey Castaneda,[d] Noel Marichalar,[d] Isaac Muench,[d] Calvin Nash,[d] Raymond Brown,[d] James Obermiller,[d] Garath Vetters,[d] and Ekam Singh[o].

a.) Department of Physics, Portland Community College, 12000 SW 49th Ave., Portland, OR 97219, b.) San Diego, CA, c.) Dallas, OR, d.) Department of Physics and Geosciences, Angelo State University, 2601 W Ave. N, San Angelo, TX 76909, e.) London, England, UK f.) Department of Physics, Cavendish Laboratory, Cambridge University, JJ Thomson Ave., Cambridge CB3 0HE, UK, g.) Department of Physics, Willamette University, 900 State St., Salem, OR 97301 h.) Department of Physical Sciences,, Linn-Benton Community College, 6500 Pacific Blvd. SW., Albany, OR, 97321, i) Reliance, TN, j.) Department of Physics, The University of Texas at Dallas, 800 West Campbell Rd., Richardson, Texas 75080, k.) School of Computing & Information Sciences, Willamette University, 900 State St., Salem, OR 97301, l.) Damascus, OR, m.) Department of Natural Sciences, Oregon Institute of Technology, 3201 Campus Dr., Klamath Falls, OR 97601, n.) Sunriver Nature Center & Observatory, 57245 River Rd., Sunriver, OR 97707, o.) Department of Computational Applied Mathematics and Operations Research, Rice University, 6100 Main St., Houston, TX, 77005.

Abstract:

The purpose of the MEE2024 project was to acquire astronomical images during the April 8, 2024 total eclipse. The precise apparent location of stars near the Sun could be analyzed to determine their gravitational deflections, and thus the Einstein coefficient of General Relativity. MEE2024 was attempted by a total of thirteen telescope stations at three locations across the central path of the eclipse. The seven stations in Texas were totally clouded out, but one station in central México had modest success, capturing 171 stars in the 4.5 minutes of totality. The team of professors, amateur astronomers, and 34 students from several colleges showed that, with planning and practice, students can acquire data to measure the Einstein coefficient. This paper describes the final results obtained by the one station in México, along with a detailed description of the data analysis software specifically written for this project. We also include lessons learned and offer equipment and procedural suggestions for MEE2027, to take place in Egypt on August 2, 2027. This paper is a call for interested parties to join the MEE2027@groups.io discussion.

Introduction:

In his early explorations of the consequences of the still nascent theory of general relativity, Einstein (1911) predicted that the path of a beam of light traveling past a massive body would curve. Despite an early misstep in 1911 that led to his missing a factor of 2, eventually he would arrive at the now accepted expression for the angle by which the light ray would be deflected, Equation 1 (Einstein, 1916). Specifically, he concluded that a ray of light passing near the limb of the sun would be gravitationally deflected by an angle:

$$\Delta\theta = \frac{4GM_{\odot}}{R_{\odot}c^2}\,\frac{1}{R} \qquad (1)$$

where G is the universal gravitational constant, $M_{\odot}$ and $R_{\odot}$ are the solar mass and radius, c is the speed of light in vacuum, and R is the distance from the center of the Sun in solar radii. Because of this, when a star is close to the disc of the Sun in the sky, its apparent angular position will change by $\Delta\theta$ as shown in Equation 1. The combination of parameters $L = 4GM_{\odot}/R_{\odot}c^2$ is called the Einstein constant and has a numerical value of 1.752 arcseconds. Besides being a very small effect, measuring the bending of starlight around the Sun poses the particular challenge that under most conditions stars that are near the Sun in the sky are too dim to observe over the Sun's glare. Therefore, scientists found they had to wait until a solar eclipse (when the disc of the Sun would be blocked by the Moon and stars would become visible) to look for evidence of this effect.

Early attempts to test Einstein's predictions (Campbell & Curtis, 1914; Perrine, 1923) were thwarted by weather and the onset of World War I and it was not until the total eclipse of May, 29th, 1919 that Einstein's prediction could be put to the test (Earman & Glymour, 1980). On that day, twin expeditions (one to the island of Príncipe in West Africa and the other to the town of Sobral in northern Brazil) organized by Sir Frank W. Dyson and Sir Arthur S. Eddington were able to capture two plates in which they were able to measure the apparent change in position for seven stars, which they found to be consistent with Einstein's predictions (Dyson et al., 1920).[1]

[1] Although this view has recently been challenged (see, e.g., Kennefick, 2012 and Schindler, 2013), some historians of science (Earman & Glymour, 1980) have argued that Eddington and Dyson may have been somewhat generous in their interpretation of the data and that they excluded data from the Príncipe site because it did not support Einstein's prediction. For entertaining historical accounts of the expeditions see the excellent books by Gates & Pelletier (2019) and by Kennefick (2021).

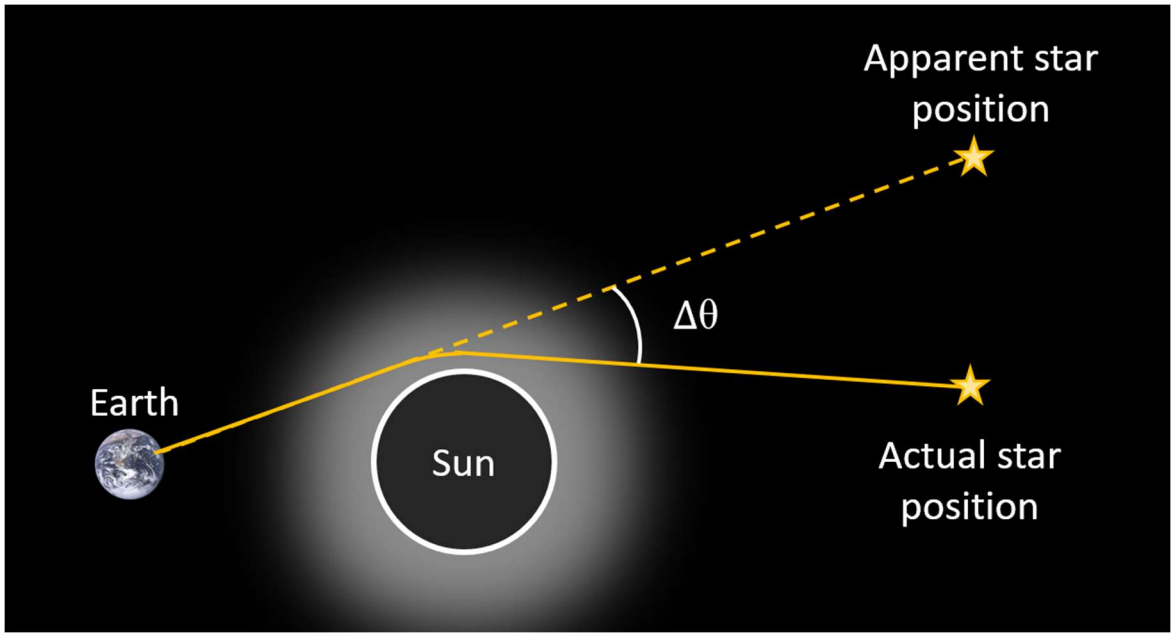

Figure 1: Schematic representation of the bending of a beam of light as it passes near the disc of the Sun. Because of this deflection the apparent position of the star in the sky appears to change by an angle $\Delta\theta$.

In the decades following the so-called Eddington Experiment, a number of expeditions were launched to reproduce and improve on the original result (von Klüber, 1960; Will, 2015). After a team from the University of Texas was moderately successful in 1973 (Brune Jr. et al., 1976), there was a 44 year gap with no new attempts at measuring the Einstein coefficient using ground-based optical telescopes until the Great American Eclipse of 2017.[2] In that year, modern digital cameras were used by several parties, ushering in the era of the Modern Eddington Experiment (MEE). Three MEE experiments in 2017 were successful – Bruns at a 7840 foot elevation on Casper Mountain in Wyoming (Bruns 2018), Kinne (set up near Bruns on Casper Mountain), and Berry and Dittrich with four undergraduate students at the Alpaca Meadows Observatory near Lyons, Oregon. Each of these teams used small refractor telescopes and CCD cameras to acquire ~ 40 images of a few dozen stars near the disk of the Sun. Bruns obtained a data set that became the most accurate measurement in history, obtaining the Einstein coefficient of exactly L = 1.752 arcsec, with an uncertainty of 3%. The data from Kinne gave a result of 2.03 arcsec, while the data obtained by Berry/Dittrich resulted in a value of 1.68 arcsec. Importantly, the experiment performed by students under the guidance of Berry demonstrated that this very challenging experiment could be performed by undergraduate students. This gave impetus for the creation of teams to repeat the experiment during the total

[2] Note that this is in part because of high precision measurements of the gravitational deflection of light made possible by radio telescope arrays (Lebach et al., 1995; Fomalont et al., 2009) and space-based telescopes (Froeschlé, 1997), as well as measurements of the Einstein coefficient using so-called Shapiro time-delay experiments (Shapiro, 1964; Reasenberg et al., 1979; Bertotti et al., 2003). For a detailed summary of the experimental evidence in support of the theory of relativity, see C.M. Will's extensive review (2014).

eclipse of 2024. Leading up to the eclipse, a paper was published (Dittrich et al., 2024) outlining the goals and methods of the experiment, which was given the name MEE2024. The teams performing MEE2024 were located at several locations along the eclipse path. The current paper reports the results and conclusions from the data they obtained. Lessons learned and suggestions for optimizing the equipment and procedures for the 2027 eclipse are also presented.

April 8, 2024 Locations:

In preparation for the eclipse thirteen telescope/camera stations were organized. These were led by faculty from several universities, as well as staff from public observatories and amateur astronomers, and operated by students, who trained with the equipment during the months leading up to the eclipse. The eclipse first passed over a team with 20 participants led by W. A. Dittrich and D. Borerro-Echeverry located at a site east of El Salto, Durango, México (23°50'58.4" N 105°16'22.0" W) at an elevation of 7930 feet. For an account of the eclipse day at the El Salto site and the events leading up to it, see Patel (2024). Then, the shadow arrived at a single telescope station operated by J. M. Izen at a location near Ciudad Canatlán, Durango, México. The eclipse finally reached the third location with 24 experimenters and 7 stations in Leakey, Texas, organized by G. Mulder and H. Hill and K. Carrell. Several additional independent amateur astronomers were also present at the Texas site.

Unfortunately, on April 8, 2024 a rare meteorological condition came across the southern eclipse path, with a subtropical jet stream bringing middle and high clouds across northern México. At Ciudad Canatlán, a gust of high wind blew the equipment onto the ground and ended the data acquisition before totality began. At El Salto, the middle clouds passed away from the eclipsed Sun five minutes before totality, leaving only areas of high cirrus over most of the sky. This reduced the acquisition of data but did not completely stop imaging. Unfortunately, complete cloud cover in Texas resulted in no eclipse images at all. The choice of El Salto turned out to be fortuitous and the results garnered from these data are described below.

MEE2024 Equipment:

The primary components of the stations were the telescopes and cameras, placed on a variety of computer-controlled telescope mounts. The team at El Salto used five Tele Vue NP101is telescopes. One of these, dubbed Station 1 and which will be the main focus of this paper, was equipped with a ZWO ASI6200MM Pro wide-field CMOS camera. The ASI6200MM Pro is a full-frame camera with $\sim$ 61 Mpx resolution. The other four telescopes, dubbed Stations 2-5, were equipped with ZWO ASI1600MM Pro CMOS cameras. In order to minimize chromatic aberration and atmospheric refraction and to block some of the short wavelength light from the solar corona, these telescopes were equipped with red filters (Edmund Optics, Part no. 89819) with a pass band from 550 nm to 700 nm. The Ciudad Canatlán setup used an Explore Scientific ED102 refractor with a Player One ZEUS 455M Pro camera. The telescopes in Texas included two Tele Vue NP101is, two Tele Vue TV-85, one Askar FRA500, one SharpStar 94ED, and one Askar

65PHQ. The cameras in Texas included ZWO ASI1600MM, ASI2600MM, ASI6200MM, ASI183MM and ASI294MM models. While eclipse data was not acquired in Texas, successful night-time distortion calibration images were analyzed to suggest the best equipment combinations for future eclipses.

Goals of MEE2024:

The central goals of the MEE2024 experiment were to:

- Utilize modern CMOS cameras to collect more data than ever before
- Maximize the number of stations to increase the data set
- Increase the number of students, faculty, and citizen astronomers participating
- Use multiple locations to minimize the chance of being clouded out
- Create an open source data processing program
- Perform the Eddington experiment more accurately than ever before
- Obtain images of stars within the Forbidden Zone (i.e., the region within 1-2 solar radii from the disk of the Sun)

The outcome of these goals will be assessed below.

Data Collected in MEE2024:

Since the Leakey Texas team was clouded out and the station in Torreón, México was disrupted by wind, data was only collected by the El Salto team with the five stations that were there. Station 1 was the large-field ZWO ASI6200MM camera and Stations 2-5 were with ZWO ASI1600MM cameras. Just before totality Station 4 lost polar alignment and could not track properly so no useful data was obtained. The data that are available from each station are shown in Table 1.

Table 1: Summary of data collected in 2024

	Images	**Exposure [ms]**	**File Size [GB]**
Station 1			
Eclipse Field	124	250	2.9
	124	300	2.9
	123	400	2.9
	124	300	2.9
Zenith Calibration Fields	680	1000	78.9

Station 2			
Eclipse Field	1498	75	46.8
	1478	100	46.2
Zenith Calibration Fields	600	1000	18.8
Station 3			
Eclipse Field	380	1000	11.9
	1202	100	37.6
Zenith Calibration Fields	600	1000	18.8
Station 5			
Eclipse Field	1202	100	37.6
	918	125	28.7
Zenith Calibration Fields	640	1000	20.0
Total:			
Eclipse Fields	7173		208.8
Zenith Calibration Fields	2520		136.5

As a result of the use of modern CMOS cameras with short download times, a total of 7173 images were captured of the eclipse field for a total file size of 208.8 GB. The original Eddington Experiment in 1919 obtained only two images with seven stars each. A 1922 experiment collected “over 100 stars on several plates of glass 14 by 17 inches in size and ¼ inch thick” (Campbell, 1923; Campbell & Trumpler, 1923). Again in 1952 a small number of plates were collected with a few dozen stars (van Biesbroeck, 1953). In 1973, the experiment obtained similar numbers of plates and stars (Brune Jr. et al, 1976). Finally, in 2017 Bruns conducted the most precise version of the experiment performed to date, obtaining 45 images with 20 stars (Bruns, 2018), with an integrated exposure time of 22 sec. Nearly 300 stars could be identified. In addition to the huge file of eclipse images, 2520 zenith calibration images were collected with a file size of 136.5 GB. Because the collection of data to be processed was so large, the creation of the data processing software described below was essential.

This data is stored securely on an iDrive account, and multiple external hard drives held by the participants. The best data came from Station 1, and this data is available open source on the website www.ModernEddingtonExperiment.org.

MEE2024 Data Processing Software:

The MEE2024 data analysis software was written in Python by A. Smith and D. Smith. The source code is posted on GitHub (A. Smith & D. Smith, 2024). Windows executable versions of the software were also created to make it easier for people to use, as configuring the correct Python environment requires some expertise.

The goals for the development of the MEE2024 software were the following:

1. Develop a robust centroid finder that could operate under a variety of conditions: night-time calibration, full-moon calibration, and during total solar eclipse.
2. Rapid and automatic stacking of a large number of FITS files.
3. Blind plate solving for a wide range of field of views.
4. Automatic matching of detected centroids to the Gaia star catalog (Prusti et al., 2016; Brown et al., 2018)
5. Correction of standard astronomical distortions: stellar aberration, parallax, and refraction (Tatum, 2024).
6. Calculation of the optical distortion of the telescope using a polynomial basis by comparison of a night-time calibration to the Gaia catalog.
7. Generation of eclipse-day plate-scale corrections using fields away from the Sun.
8. Creation of a list of placement errors for the Sun-centered centroids, taking into account the known sources of error.
9. Least squares fit using the Einstein coefficient (L) and the location of the center of the Sun.

Together these features provide a single integrated software package to perform the analysis conducted by Bruns in 2018, who originally used several commercial software packages (MaxIm DL, Astrometrica, NOVAS, etc). The disadvantage of using commercial software is that it is challenging or impossible to alter the code or even fully understand some of its functions. The software licenses can also be expensive and the software itself can be difficult to learn to use.

During the development of the MEE2024 software, we used Bruns' calibration and eclipse data from the 2017 eclipse. We were able to do a full analysis of his 2017 data in a few hours and obtained a result that closely matched his published results.

The workflow for the analysis of data outlined above using the MEE2024 software is broken down into three "Tabs" in the user interface (UI). Tab 1, shown in Figure 2, allows the user to configure and execute the centroid finding, image stacking, and initial plate solving steps (1-3 above).

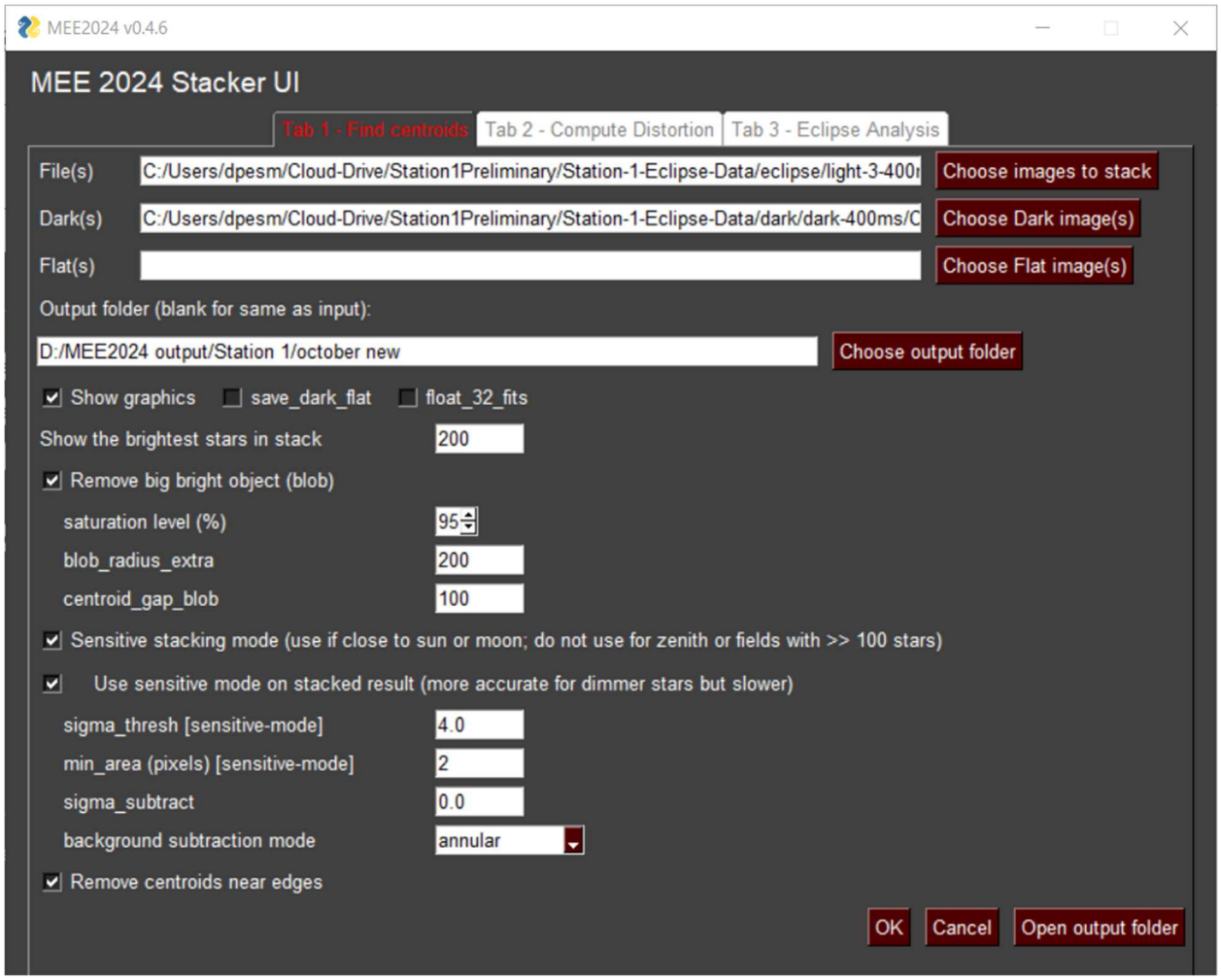

Figure 2: MEEE2024 software user interface. Tab 1 is used for finding centroids, stacking and obtaining a blind plate solution. The code uses standard Python libraries and is open source (Smith & Smith, 2024).

Several sensitivity parameters can be set for the centroid finding. Night-time data will have very high signal-to-noise since exposure times can be arbitrarily long (e.g. several seconds) and the background light can be quite low. Data taken with a full Moon or eclipsed Sun will have much higher background light so more careful centroid finding is required. In addition, the Moon and Sun need to be appropriately masked or large numbers of spurious centroids will be found. Detailed discussions of the various parameters are provided in the program's GitHub repository (Smith & Smith, 2024).

Tab 2 of the UI, shown in Figure 3, calculates the standard astronomical distortions using AstroPy (Robitaille, 2013; Price-Whelan et al., 2018; Price-Whelan et al., 2022) and calculates the position errors with respect to the Gaia catalog (steps 4-8 above).

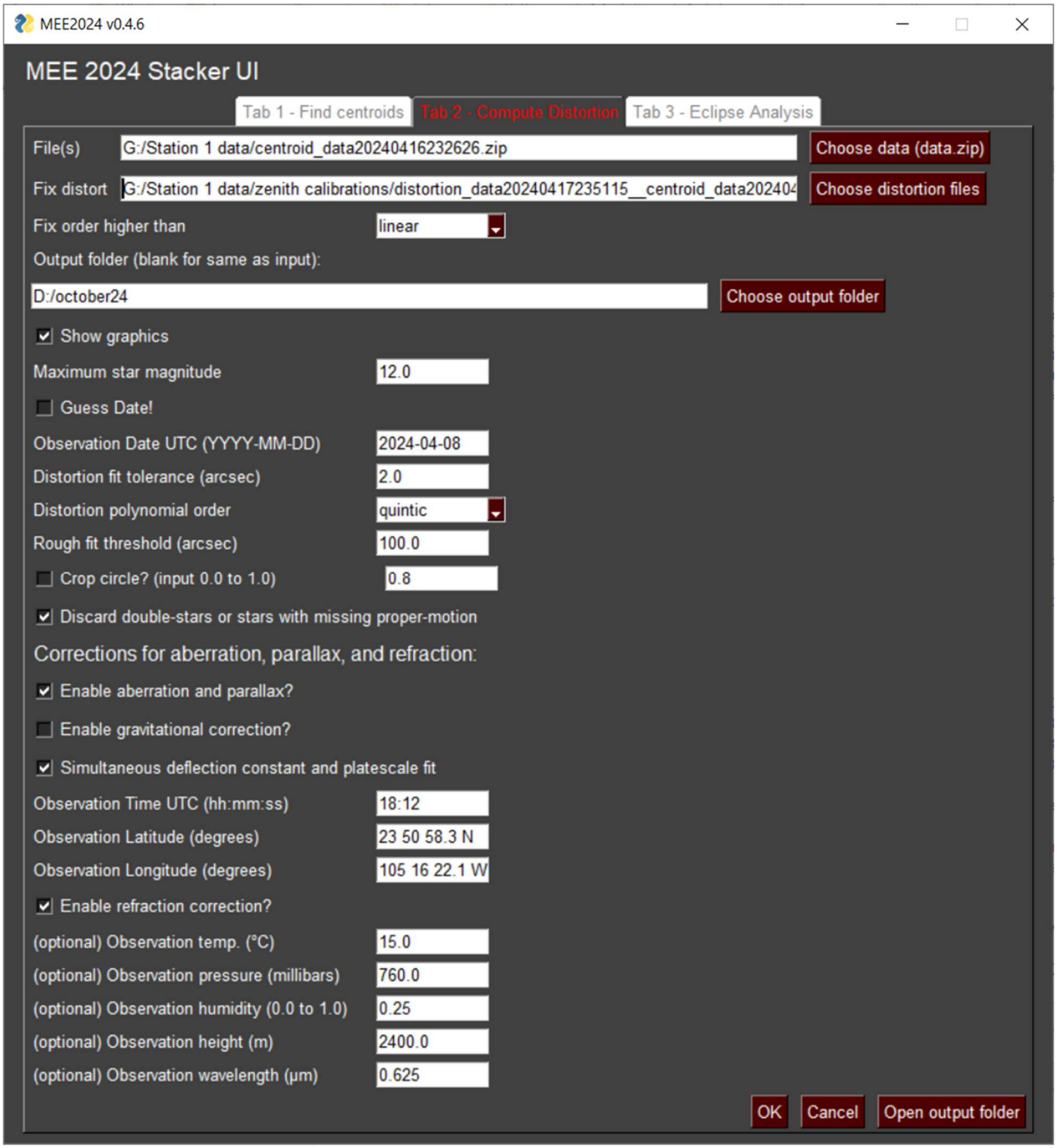

Figure 3: MEE2024 UI. Tab 2 is used for standard astrometry corrections (using AstroPy), characterizes the optical distortions of the telescope system, and applies the corrections derived from calibration frames to the eclipse frames. The output of Tab 1 is the input to Tab 2.

The workflow is to take the output of Tab 1 and enter it into Tab 2. In fact, Tab 2 is used several times: first for calibration then for the final generation of the gravitational deflections. As previously described by Bruns (2018), most good quality telescopes can be corrected sufficiently with a cubic polynomial function. However, we did find that at very wide fields of view, a significant quintic distortion is noticeable and also needs to be accounted for.

The first step is to generate the night-time distortion files. These are sometimes referred to as "zenith calibrations", although they do not need to be taken exactly at the zenith. A series of offset fields near the zenith (on the order of a dozen) are stacked in Tab 1 and in a first pass through Tab 2 generate a set of distortion calibration files. These correct for up to septic optical distortion of the telescope, although typically cubic is sufficient. In this first pass, the "Fix order higher than" toggle is set to "None". The dozen or so calibration frames can all be done at once in a batch mode. The toggle for "Simultaneous deflection constant and plate scale fit" should normally not be selected. "Enable gravitational correction" should also typically not be selected.

In Bruns' 2017 eclipse data, right and left calibration fields were taken on the day of the eclipse. This pair of stacked images is then corrected using the set of zenith calibration files. In this second pass through Tab 2, "Fix order higher than" is set to "quadratic". This means that the cubic and higher coefficients are frozen at the night-time readings, but the linear and quadratic "plate scale distortions" (typically due to thermal expansion) are recalculated. A pair of new calibration files is generated, and these are used on the stacked eclipse field data. Tab 2 is run a third time with "Fix order higher than" set to "constant". In this case, "constant" corresponds to a translation in x-y pixel space.

Note that the number of eclipse day calibration fields could be just one rather than two; or in theory it could be more than two. Generally, an even number of calibration fields taken symmetrically before and after the eclipse should give the best correction.

The case of there being no eclipse day calibration means that changes in the linear and quadratic plate scale from the night-time calibrations are not taken into account. This special case needs to be dealt with in a different way and will be discussed below.

The final output data file of Tab 2 is then entered into Tab 3, shown in Figure 4, which performs the gravitational distortion analysis (step 9 above).

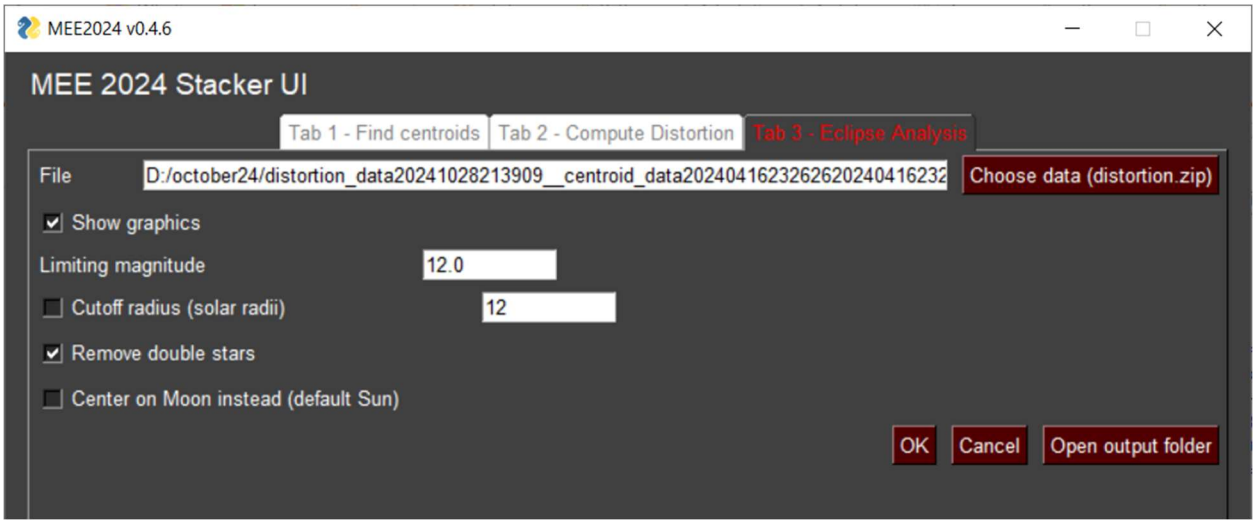

Figure 4: MEE2024 UI. Tab 3 primarily produces graphical output from the numerical output of Tab 2. This section of the software calculates the Einstein coefficient L by fitting the star deflections to a $1/R$ curve using a least-squares method.

The two “data limits” that are included in Tab 3 are stellar magnitude and the radial cutoff. The radial cutoff is meant for extremely wide fields of views where the edges of the frame can have significant errors. The stellar magnitude limit is effectively a limit on the acceptable signal-to-noise of the centroids. Higher magnitude (dimmer) stars are more difficult to locate precisely. In Tab 2 there is also a “Maximum star magnitude” feature that is used for the calibration process. For night-time calibration, a limiting magnitude of around 12 is a reasonable choice: it gives a good number of stars to generate a distortion calibration field. Adding more, but dimmer, stars could result in a worse final rms error. The same logic appears to be true for the eclipse field. Including dimmer stars means there are more stars to fit, thereby decreasing the statistical error. However, if one were to weight all the stars equally then including many low signal-to-noise centroids from dim stars means the high signal-to-noise data points are “diluted”. For both calibration and eclipse fields, there is typically a “limiting magnitude” which minimizes total residual rms error. Ideally, non-equal weights could be assigned to stars based on an estimate of their signal-to-noise ratio, but an unbiased implementation of this method is non-trivial.

Tab 2 and 3 offer the possibility to ignore close double-stars and stars which lack a proper motion correction. These are both a fairly small number of stars so unlikely to affect calibration fields, but could impact the eclipse fields.

Note that the “Center on Moon” (rather than Sun) option is for night-time full-moon calibrations. This should result in no $1/R$ dependence of the displacements (i.e. $L = 0$).

The method used by Bruns (2018) to analyze the 2017 eclipse fits the deflections to a $1/R$ function using the Einstein coefficient L and the position of the center of the eclipse image field (right ascension RA, declination DEC, and roll) as parameters to be fit using least squares. The reason for fitting the image center position is that the plate solver is not able to exactly find the center position; i.e. there is a very small initial offset error in the displacement measurements (with respect to the center of the Sun). This is the general method that Tab 3 of the software uses to find L.

In order to validate the software, we used it to analyze Bruns’ data from 2017 and found close agreement with his original results. We will now discuss this analysis as it will be helpful to understand certain aspects of our analysis of the 2024 data.

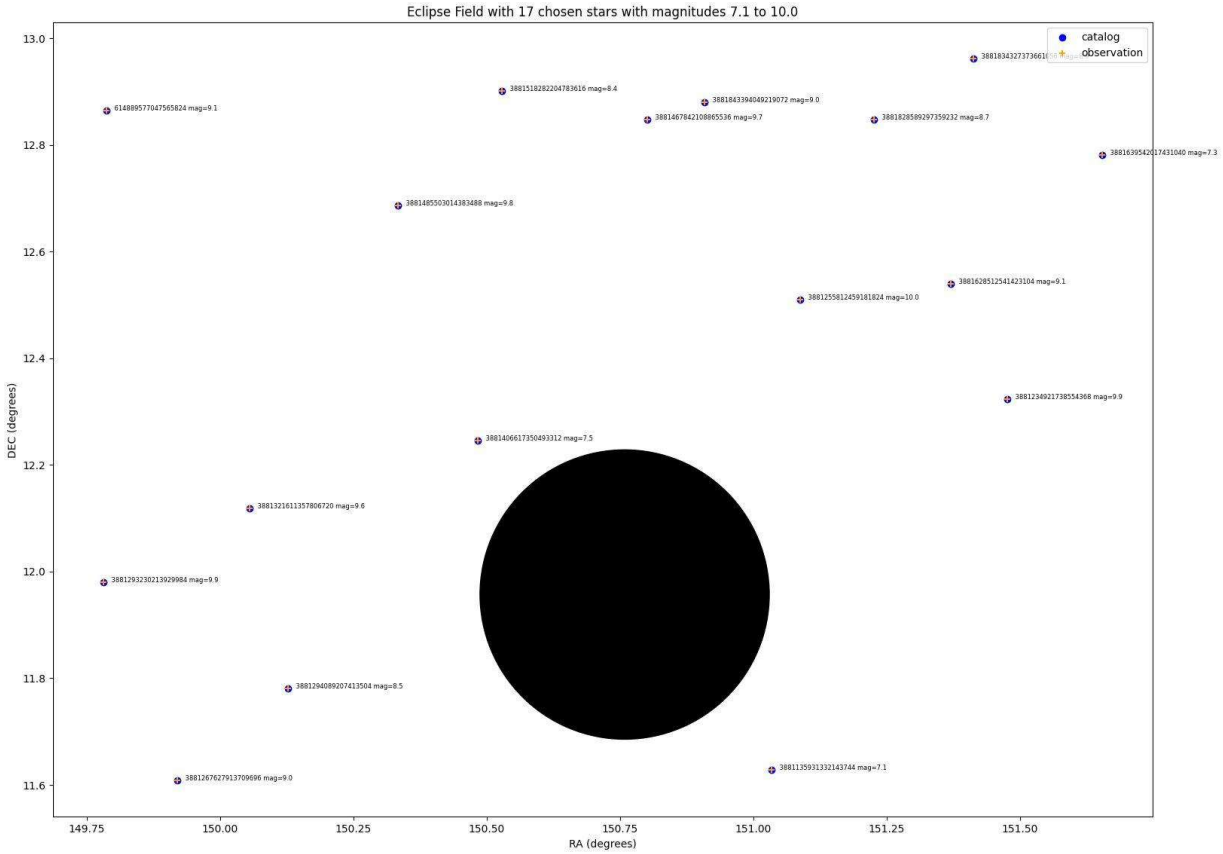

Figure 5: MEE2024 graphical output of star locations from the 2017 Bruns data. The experimental data is compared to the Gaia star catalog.

Figure 5 is a screenshot of the initial representation of the eclipse deflections. In the program, it is actually possible to zoom into individual stars and see that there is an apparent outward shift of the stars compared to the catalog positions (i.e. stars behind the Sun can in principle be visible because of the bending of their light paths; see Figure 1). In this example, we have used a limiting magnitude of 10.0, which results in 17 stars in the field of view (Bruns used 20 stars). The Gaia catalog number and the stellar magnitude are noted next to each centroid. Note that the two stars closest to the Sun (with magnitudes of 7.1 and 7.5) are amongst the three brightest stars in the whole field.

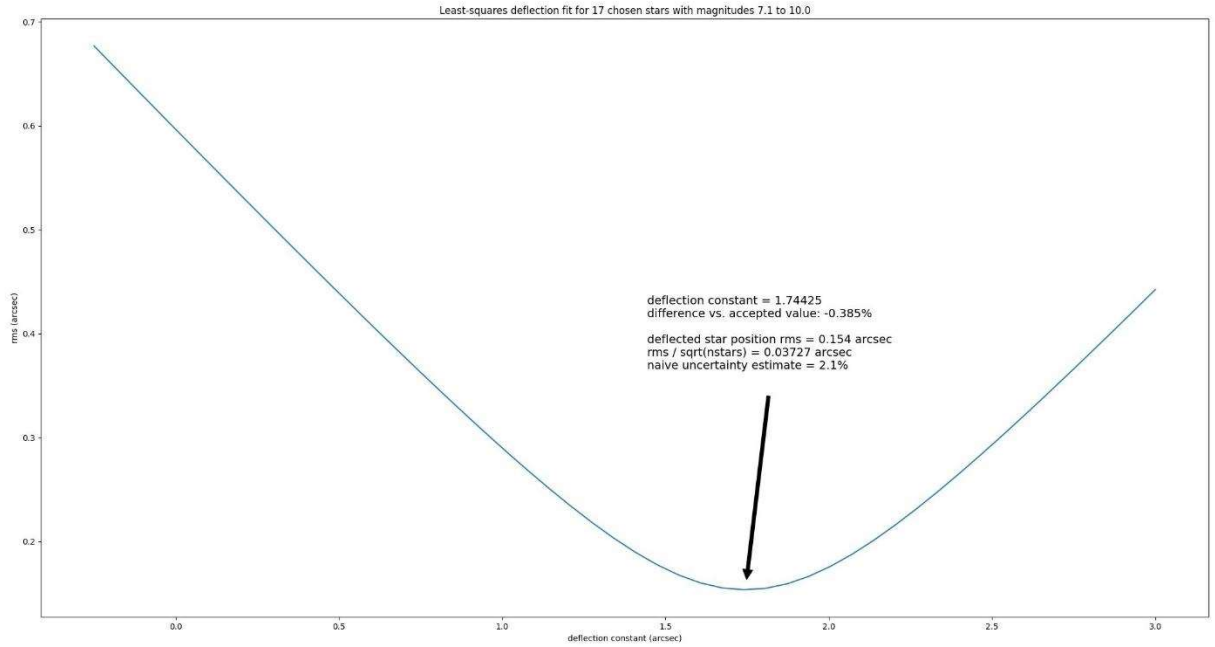

Figure 6: MEE2024 graphical output that shows how the Einstein deflection coefficient L is found by minimizing the error in fitting Bruns' 2017 data to a $1/R$ function.

Figure 6 shows how the program uses a least-squares analysis to find that the minimum aggregate error occurs at $L = 1.74425''$, only 0.4% from Einstein's prediction. A "naive uncertainty estimate" can be defined as the residual rms error divided by the square root of the number of stars. In this case, that error is 2.1%, similar to the system error calculated by Bruns (2018).

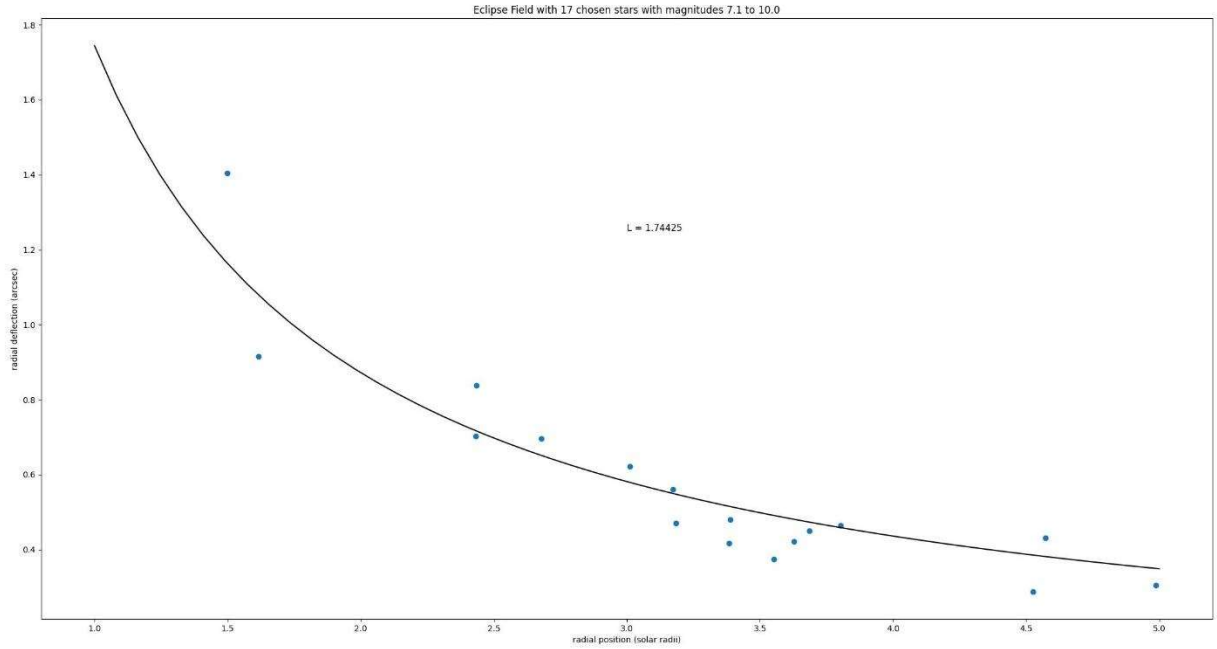

Figure 7: MEE2024 software graphical output plotting the radial deflections versus the radial position, overlaid with the derived 1/R function (Bruns' data from 2017).

Finally, Tab 3 of the program will generate a plot of the radial deflection of the stars versus their radial distance from the Sun's center and overlay the 1/R function (see Figure 7).

Analysis of MEE2024 data:

The current analysis is limited to a subset of the Station 1 data (obtained by team members Berry, Dittrich, Matin and Delgado): the 123 eclipse images taken at 400 ms exposure on April 8, 2024 and the 17 zenith fields captured the night before. Each zenith field is a stack of twenty 3 sec exposures. The total integrated eclipse exposure is 49.2 sec. Figure 8 gives an example of one zenith stack analyzed using Tab 1 of the MEE2024 software.

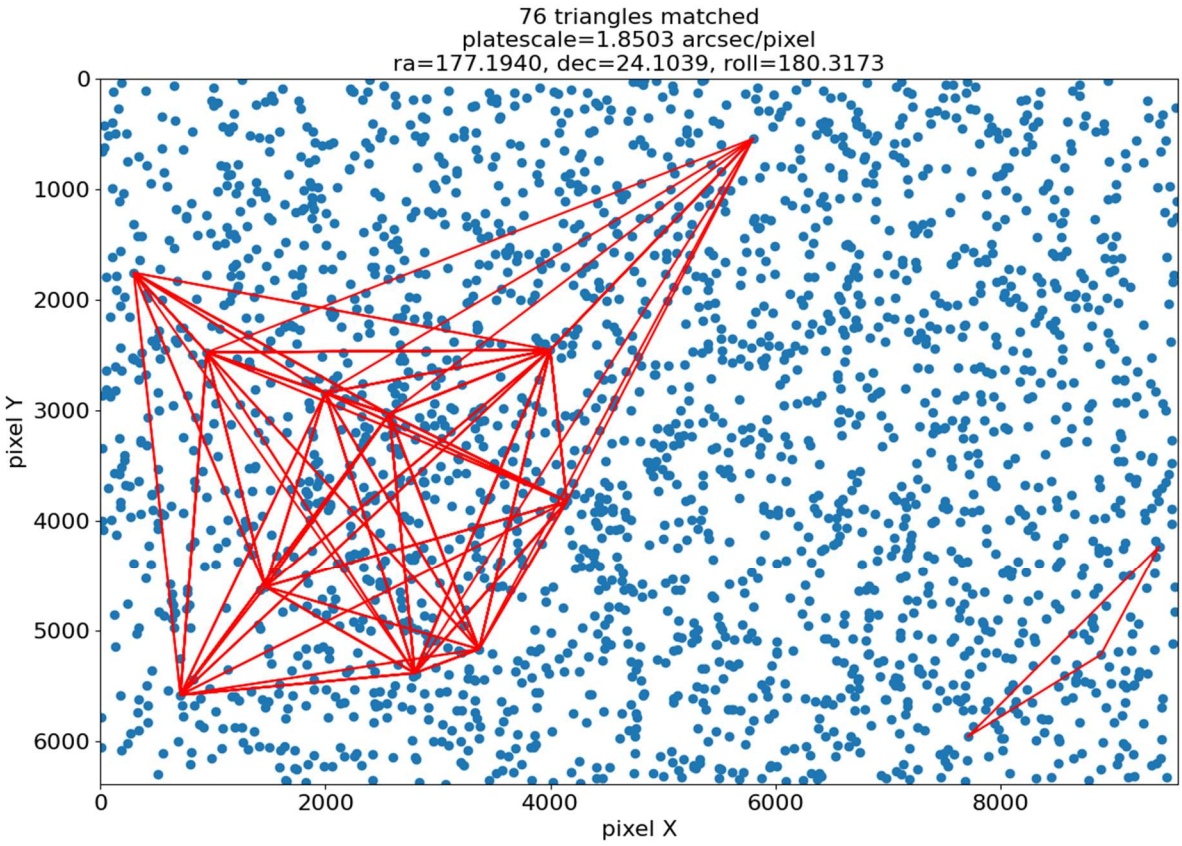

Figure 8: Sample graphical output from Tab 1 for a zenith calibration set from Station 1 at the El Salto site. Triangles (shown in red) formed from detected centroids (shown as blue dots) are matched against triangles computed from the Tycho-2 star catalog (Høg et al., 2000) to determine the field coordinates and plate scale. The blind plate solver was specially developed for the MEE2024 software package. The plate solver works very fast and is quite robust; it uses a built-in database so does not need an internet connection.

In this calibration field, 2383 centroids were found. The blind plate solver matched 76 triangles in order to find the image field coordinates and plate scale. When this centroid data is entered into Tab 2, a full quintic distortion correction is derived. In this case, a limiting magnitude of 15

was used in order to get a very high density of stars in the field of view. The more centroids that can be detected in the zenith field, the more accurate will be the fit to the optical distortion of the telescope system. A high density of centroids is particularly important if the telescope has a large and complex distortion.

To appreciate how much quintic distortion affects Station 1, Figure 9 shows a graphical representation generated by Tab 2 of the correction function computed for the zenith data above with the residuals computed for stellar centroid positions overlaid. The fit is extremely good, except perhaps in the extreme corners, where the distortion is particularly high.

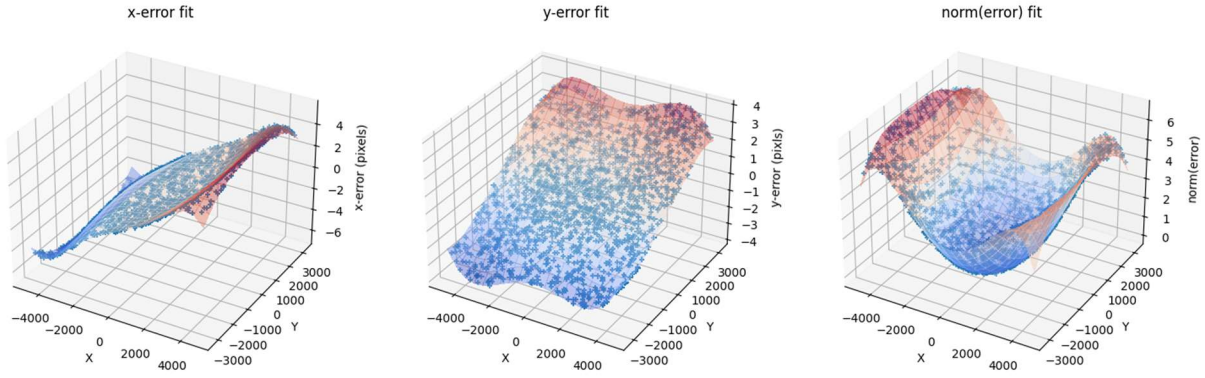

Figure 9: Example of the correction function computed for Station 1. (Left) The blue dots indicate the measured residuals Δx in the experimentally determined positions of stars along the x direction when compared to their catalog positions as function of their position in pixels relative to the center of the image. The surface shows the surface of best fit, which can be used to compensate for the distortion when measuring star positions in later experiments. While most systems can generally be corrected with a cubic function, the wide-field of Station 1 requires a quintic function. (Middle) The residuals in the y position of stars Δy along with the surface of best fit. (Right) The norm of the overall residuals $\Delta s = \sqrt{\Delta x^2 + \Delta y^2}$ as a function of position. It can be seen that the correction function can correct stellar positions well throughout the full image.

Figure 10 provides a representation of the polynomial coefficients which correspond to the distortion surface plotted in Figure 9. The form of the corrections are two polynomials:

$$x_c = x + \sum_{n=0}^{N} \sum_{i=0}^{n} A_{n,i} \alpha^i \beta^{n-i} \qquad y_c = y + \sum_{n=0}^{N} \sum_{i=0}^{n} B_{n,i} \alpha^i \beta^{n-i}$$

where (x ,y) are the initial observed centroid coordinates, (x_c, y_c) are the corrected pixel positions, while (α , β) are the shifted and scaled coordinates such that the center of the image is (0 , 0) and the long edge is at ± 1. An advantage of using scaled coordinates is that the magnitudes of the coefficients are of order unity and can be compared easily. The coefficients $A_{n,i}$ $B_{n,i}$ go up to finite order N, typically either cubic (N=3) or quintic (N=5). If one assumes there to be a perfect mirror symmetry in the distortion along the x and y axes, then only the odd order coefficients would be non-zero (n=1,3,5…) and for the $A_{n,i}$ only odd i allowed, while for $B_{n,i}$ only even i allowed. The translational, rotational, and scaling degrees of freedom (i.e. RA, DEC, roll, and plate scale) allow for four degrees of freedom to be removed from the polynomials;

we choose the convention of having $A_{00} = B_{00} = A_{11} = 0$ and $A_{10} = -B_{11}$, which means that the distortion coefficients can be uniquely determined. We observe that the mirror symmetry rule is quite well-respected empirically, except for the linear and quadratic orders, where small asymmetries in the instrument (such as lens alignment) result in non-negligible terms. We suggest it may be acceptable to set all "symmetry forbidden" coefficients (except for linear and quadratics) to zero, which would eliminate about ¾ of the degrees of freedom in the distortion fit.

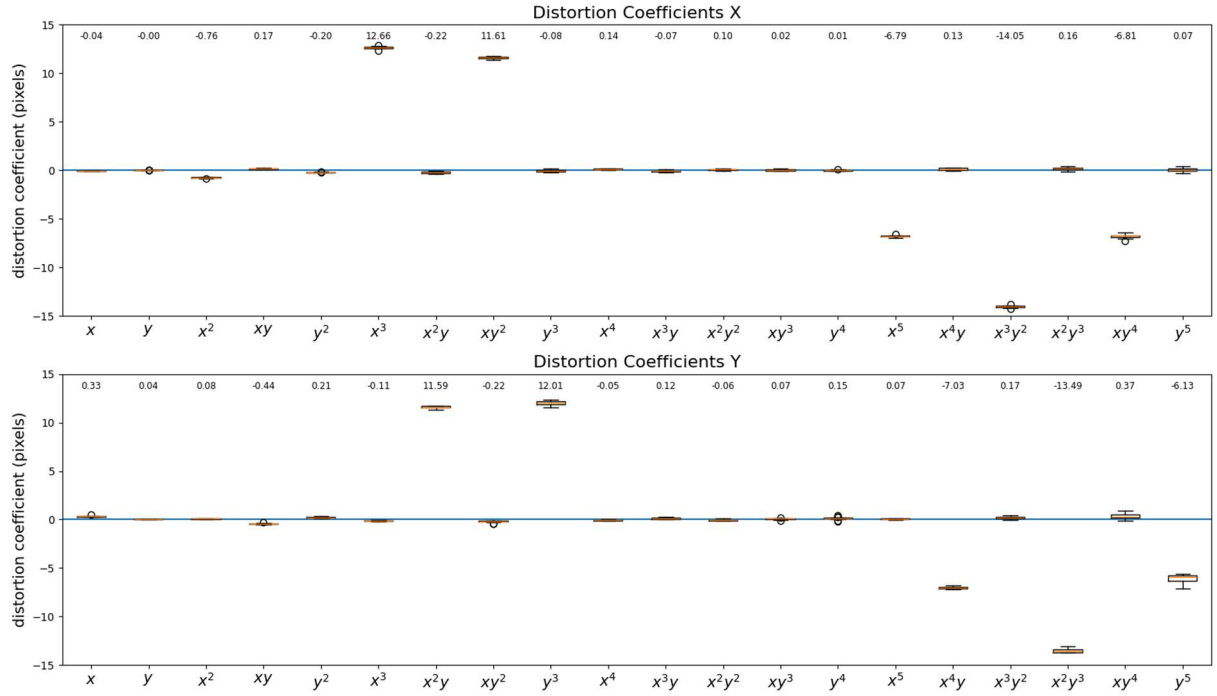

Figure 10: Graphical representation of the distortion coefficients for Station 1. The top plot shows the coefficients for the x-correction ($A_{n,i}$), while the bottom corresponds to y ($B_{n,i}$). Note that the cubic and quintic components are dominant. The quartic components are negligible, as expected by symmetry. The quadratic components are small but meaningful. The spread of values measured for 17 separate zenith calibrations is shown, demonstrating excellent stability in the fit. The mean values of each coefficient is printed along the top.

Figure 11 provides a few useful plots of the residuals obtained by comparing the experimentally measured positions of stars to their known positions from the Gaia catalog (Prusti et al., 2016; Brown et al., 2018). As can be seen, the residuals are fairly insensitive to a variety of factors, including the star magnitude, parallax, and radial distance from the center of the image.

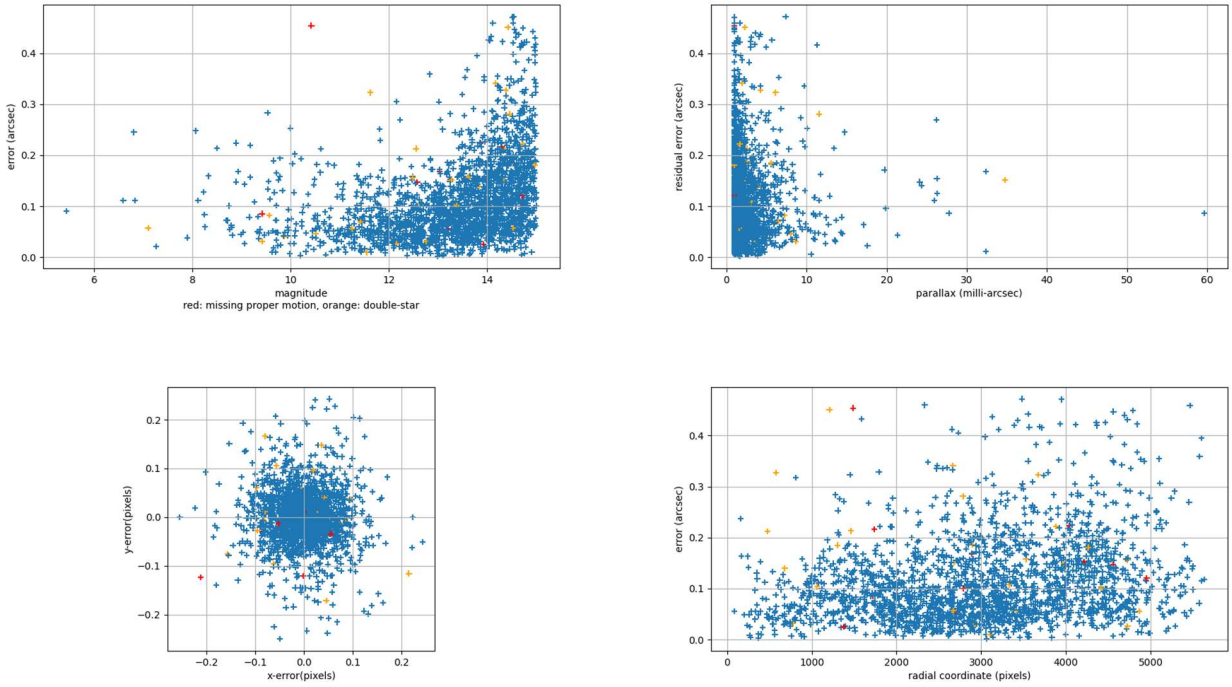

Figure 11: Scatter plots showing the random (and potentially systematic) errors in a zenith calibration from Station 1. Stars for which proper motion information is missing in the Gaia catalog are highlighted in red. Double stars, which can potentially lead to centroids with higher error, are marked in orange. (Top left) Residual error as a function of star magnitude. The residual error increases significantly with magnitude; there are also many more dim stars (mag 14) than bright ones (mag 7). (Top right) There is very little dependence of the residuals on parallax angle (i.e., distance from the Sun) (Bottom left) The scatter plot of the stellar residuals in x and y is symmetric (helping to exclude the possibility of a systematic bias) and generally shows that the rms positions of the centroids can be corrected to within 0.14 pixels of their theoretical catalog positions. (Bottom right) A plot of the residuals as a function of radial distance from the center of the image shows that the calibration works well all the way to the edge of the image.

The stacking of the 123 frames taken at 400 ms exposure was done similarly to the test run done on Bruns' 2017 dataset. Figure 12 shows the stars used for stacking and the number of times that star appeared in the 123-frame dataset (122 is actually the maximum times a match can occur with respect to a reference frame):

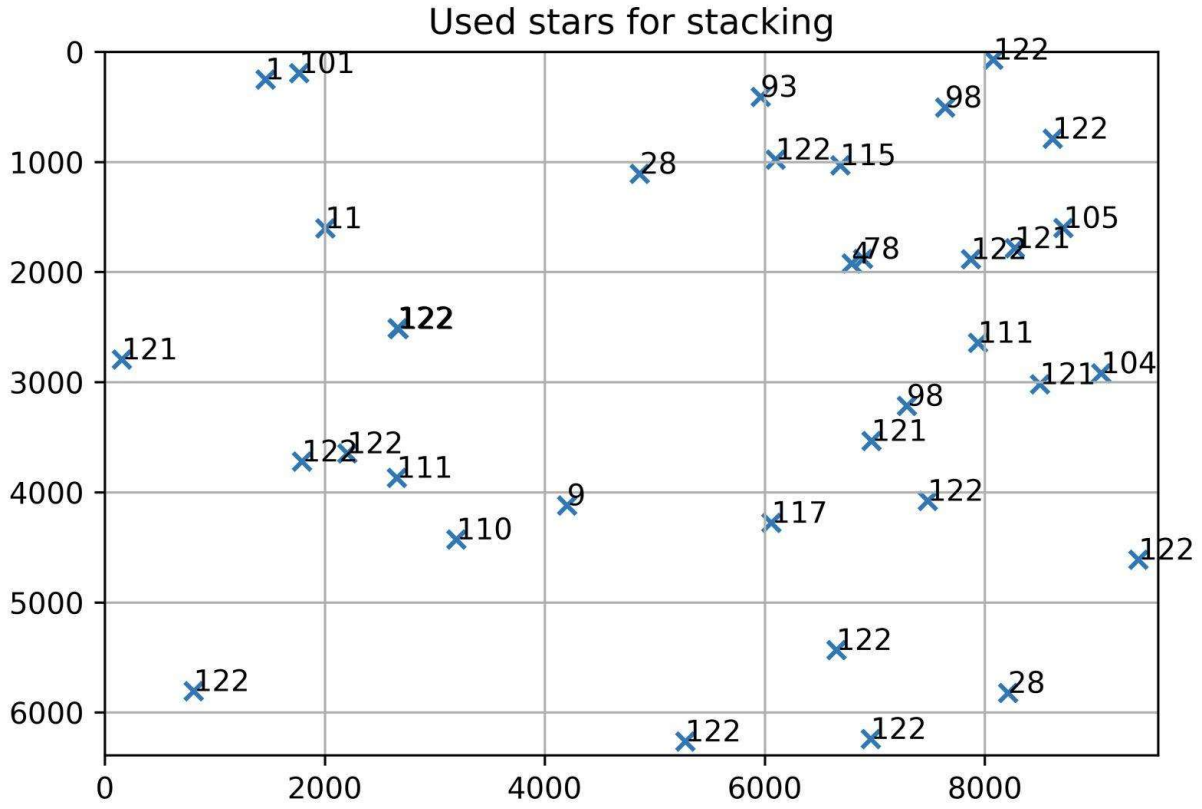

Figure 12: Example of the multi-star stacking implemented in the MEE2024 software. We believe that the multi-star method is more likely to give better results than a single-star method.

The program then proceeded to plate solve the stacked image and was able to correctly identify the eclipse location. 276 centroids were found in the stacked image and the program's in-built star catalog (derived from Tycho-2) could identify 99 with brightness down to magnitude 11, as shown in Figure 12.

One of the objectives of MEE2024 was to test the feasibility of using a full-frame camera sensor to capture images of stars over a wide angular field of view. This avoids slewing the telescope between different fields, which can add complexity and consume valuable observation time. In Bruns' 2017 measurements, the telescope slewed to either side of the eclipse field where gravitational deflections in stellar positions were small. As explained above, these calibration fields are used to correct the linear and quadratic distortion terms of the telescope system under similar thermal and orientational conditions to when the eclipse field is imaged.

During MEE2024, Station 1 did not slew during the eclipse, so no eclipse-day calibration data were available to refine the linear and quadratic distortion terms from their night-time values. To get around this, we chose to use the quadratic, cubic, quartic and quintic terms of the zenith calibrations taken the night before, leaving only the linear terms to be adjusted from the eclipse star field. The rationale behind this is that the linear plate scale terms are most sensitive to the thermal difference between the night-time calibration and the daytime measurement. In the

software, this is done by loading output of the distortion calculation from the previous night's zenith observations and adjusting the "Fix order higher than" setting in Tab 2 to "linear".

As pointed out by Freundlich and Lederman (1944), it is highly desirable to have an independent determination of the plate scale: "The inclusion of a scale correction S and of L as unknowns in the Least Square solution has to be avoided. . . The scale correction has therefore to be determined separately." In the case where the plate scale and the deflection constant are both unknowns in the least-squares solution, then the largest possible number of stars should be used. Fortunately, the stack of 400 ms exposures from Station 1 contains a very large number of stars.

Mikhailov (1959) discussed the important eclipse data taken between 1919 and 1952. It was common in the early experiments to have no independent plate scale since the telescopes were too large to be slewed. Mikhailov (1959) describes the problem as a shift of the stars in a radial direction by an amount ΔR caused by the plate scale uncertainty, with ΔR expressed in arcseconds. Therefore the expression for the radial displacement of each star is $\Delta R = A/R + BR$, where the two constants A and B are to be determined by a least-squares method. The constant B is mainly obtained from stars with large values of R, while the constant A is determined mainly from stars with small values of R. The distant stars should be at least 6 to 8 solar radii away, requiring a field of view of at least 4 degrees. (The A and B constants of Mikhailov are equivalent to L and S from Freundlich and Lederman).

In a sense, MEE2024 Station 1 is a hybrid experiment: modern in its acquisition technology but classical in its data taking strategy. The analysis was therefore also hybrid: done along the lines presented by Mikhailov (1959) but using comparison to the Gaia star catalog. As shown in Figure 13, Station 1 could observe a field going out to 11 solar radii, with over 170 stars. This field is as large as the historical experiments but with a much greater number of stars (see Table 1, Mikhailov (1959)). As a result, despite not having an external plate scale calibration, we believe that we were able to determine L to within 5% of the accepted value of 1.75 arcsec. Nevertheless, one of our conclusions is that an even higher accuracy would have been achieved if at least one external calibration field had been taken.

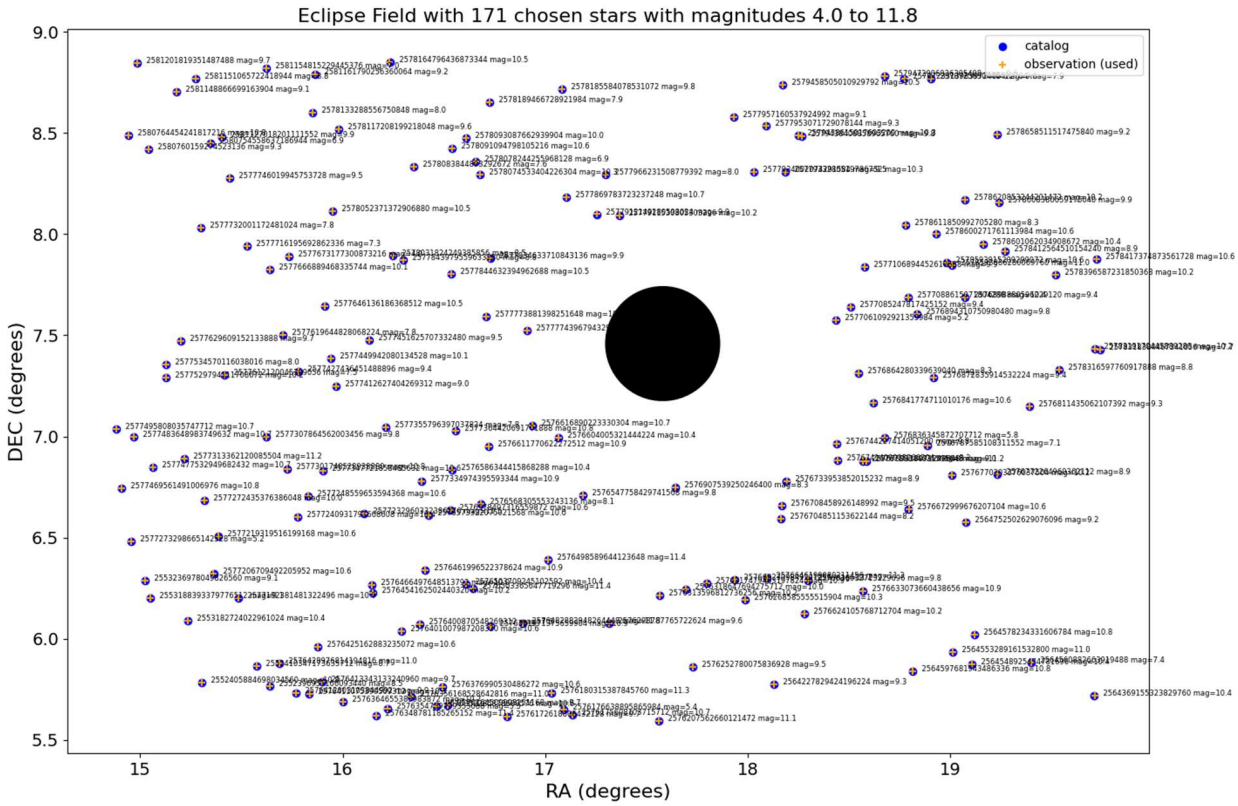

Figure 13: The star deflections during MEE2024 from the Station 1 data. This dataset is from the 123 frames taken at 400 ms exposure (total exposure of 49.2 sec). Star brightness down to 12th magnitude was used.

To get a large number of stars, we used a limiting magnitude of 12. As mentioned above, magnitude 12 is a good value for night-time calibrations and we would normally limit the eclipse-day stars to between magnitude 10 and 11. In our analysis of Bruns' 2017 data, we used a magnitude 10 limit (Figures 5-7). As shown in the top left part of Figure 11, the error in star location starts to rise considerably above magnitude 13. There are obviously more stars at higher magnitudes than at lower, but the dimmer stars have worse signal-to-noise so they cannot be located as precisely.

In Tab 2, we used a large "Distortion fit tolerance" of 2.0 arcsec and a large "Rough fit threshold" of 100 arcsec in order to not exclude any centroids (see Figure 3). We also did not use "Crop circle", which would have excluded stars in the corners. We think the quintic distortion correction was sufficient at the corners as the error at the edge of the frame did not get noticeably worse (bottom right part of Figure 11). In Tab 3, we also did not limit the magnitude of the stars or use a cutoff radius (see Figure 4). We did, however, use the double star removal option.

Once the centroids were matched to the Gaia star catalog and the positional errors found, a statistical method was used to vary the plate scale and deflection constant. Importantly, the toggle for "Simultaneous deflection constant and plate scale fit" in Tab 2 was selected (see Figure 3). After an approximate plate scale was found from Tab 2, Tab 3 was used to perform a

least squares regression on the observed radial deflections from the Sun using Mikhailov's equation $\Delta R = A/R + BR$. This effectively allowed a simultaneous refinement of the plate scale measurement and the deflection constant. Using this method, the standard statistical Bayesian uncertainty and covariance of the plate scale and deflection constant could be easily computed. We found that the estimated errors in L and plate scale were strongly negatively correlated (correlation = neg 0.783), as can be seen in Figure 14. This intuitively represents the fact that a decrease in plate scale results in an apparent displacement similar in effect to an increase in deflection constant. If the plate scale was known exactly, the uncertainty in L could be reduced by around a factor of two, demonstrating the importance of taking calibration fields.

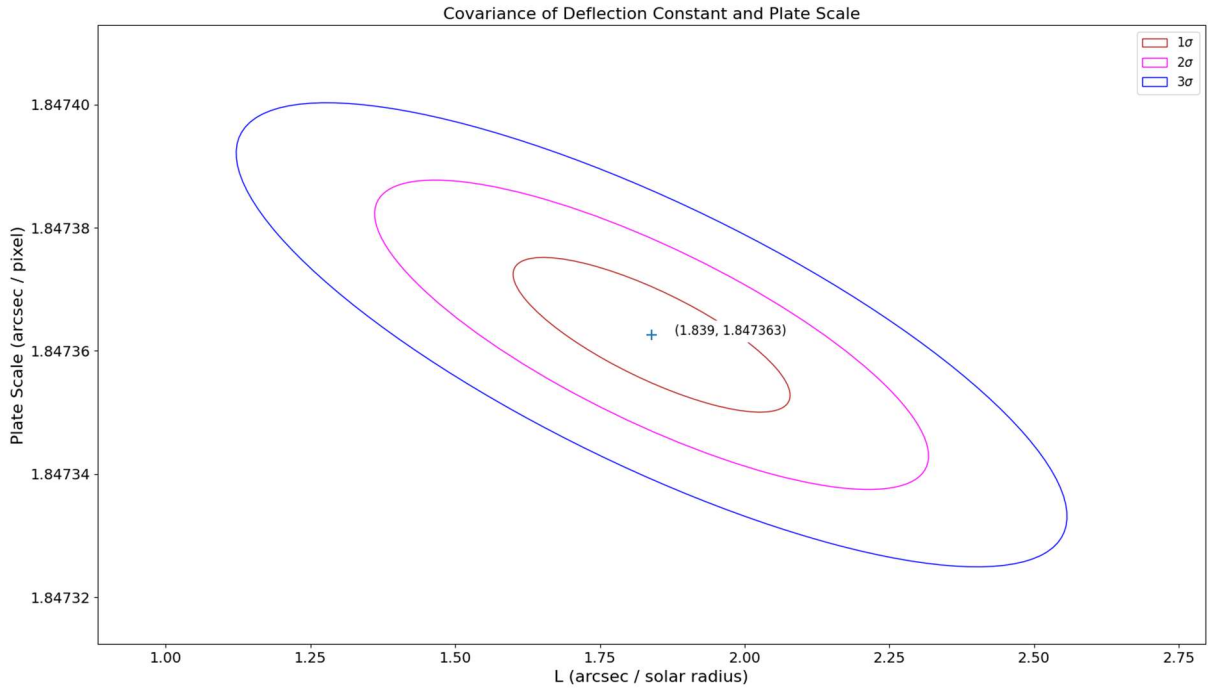

Figure 14: Covariance method for determining the deflection constant with an uncertain plate scale. For the Station 1 data, a value of L = 1.839 arcsec is found, with a 1 sigma error of 0.239. The plate scale result is 1.847363 arcsec/pixel, with a 1 sigma error of 1.3E-5.

The value of the deflection coefficient of L = 1.839 arcsec is 5% greater than the accepted value of 1.75 arcsec. Interestingly, when Bruns analyzed his 2017 data using only the eclipse field (ignoring the independent plate scale derived from the two calibration fields), he found L = 1.86 arcsec, an error of 6%. From Table 1 of Mikhailov (1959), the most similar historical experiment to Station 1 is the 1922 Lick Observatory expedition to Australia. Mikhailov's reanalysis of the Lick data showed 71 stars at distances of 2.1 to 13.0 solar radii, with L = 1.83 arcsec. The clustering of these three calculations within a range of 0.03 arcsec is intriguing and may even suggest a systematic error in this method of data analysis.

When we use the value of L found in Figure 14 and replot the radial deflections versus distance from the Sun, we get the results found in Figure 15. It is immediately apparent that the scatter in the data points is quite large, especially when compared to Figure 7, the similar plot of Bruns' 2017 data. Observers at the site in Mexico noted that there was high wind and intermittent

clouds, which may have caused a much higher level of air turbulence and therefore higher centroid error than was seen in the night-time zenith calibrations when the air was very still. Nevertheless, the very large dataset of 171 stars appears to allow averaging out the large random errors to arrive at a value of L that is off by only a few percent.

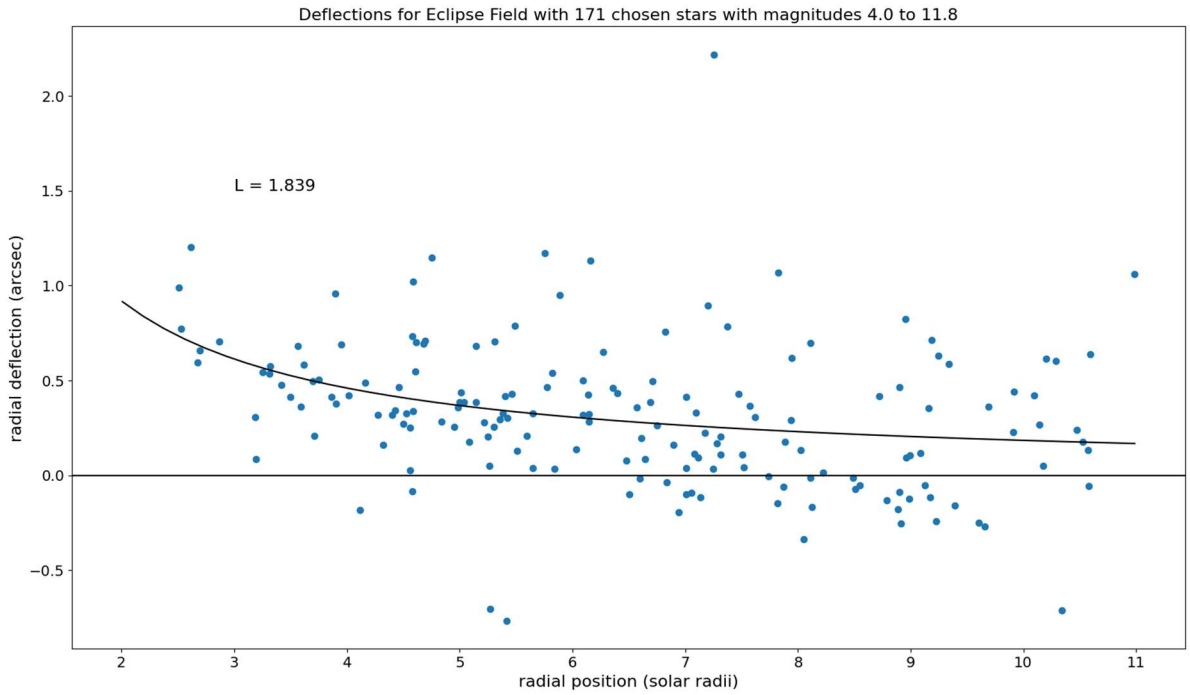

Figure 15: The plot of radial deflections versus radial position shows a large amount of scatter and no stars closer than 2.5 radii (compare with Figure 7, the similar plot from the 2017 Bruns data).

Note also that there were no stars detected at less than 2.5 solar radii, so stars with very high deflections were not in the 400 ms dataset. We did an analysis of the 250 ms Station 1 dataset to see if any closer stars could be identified. In fact, one close star was found, Gaia 2577063532462714368, with magnitude 9.7. This relatively dim star at a distance of 1.97 radii was just visible near the solar corona at this shorter exposure. However, the signal-to-noise was quite poor and the deflection error was around 1 arcsec more than would be expected. The addition of this single close star throws off the whole calculation of L since inner stars have much higher influence on the calculation. We therefore conclude that stars close to the corona also need to be quite bright in order to be accurately located. A single close-in outlier can actually cause a significant increase in error. In the case of Bruns' 2017 data, the two inner stars were 7.1 and 7.5, over two orders of magnitude brighter.

Analysis of Optical Distortion and Optimizations:

Commercially available refractors and CMOS cameras can be used for precision wide-field astrometry when careful procedures are followed. Calibration images taken at night are used to determine the higher order optical distortions of the telescope and camera. Those coefficients are applied to the target images to measure final stellar positions with milli-arcsecond precisions. Tests with several telescopes show the optical distortion coefficients are repeatable over weeks, to within a few percent.

The following analysis shows that the Sun should be placed sequentially in all four image corners. The novel idea presented here is that only the cubic optical distortion component parallel to the deflection vector is significant. These images should take most of the totality, with the start and end of totality used to get linear calibration images (typically 10 degrees away from the Sun). This optimizes the data set.

Distortion stability measurements:

The cubic optical distortions of two refractors were repeatedly measured in the spring of 2024 on several clear nights. An NP101is telescope was paired with a ZWO ASI2600MM camera and a TV-85 (with 0.8× reducer) with an ZWO ASI1600MM camera. The results are plotted in Figure 16. The mean values for the two telescopes over all nights were 7.09 arcsecond +/- 0.9% and -1.03 arcseconds +/- 2.6%. These examples show the cubic optical distortions are stable and can be measured to within a few percent accuracy. The 1% to 3% stability of both telescopes is expected to apply to the other designs.

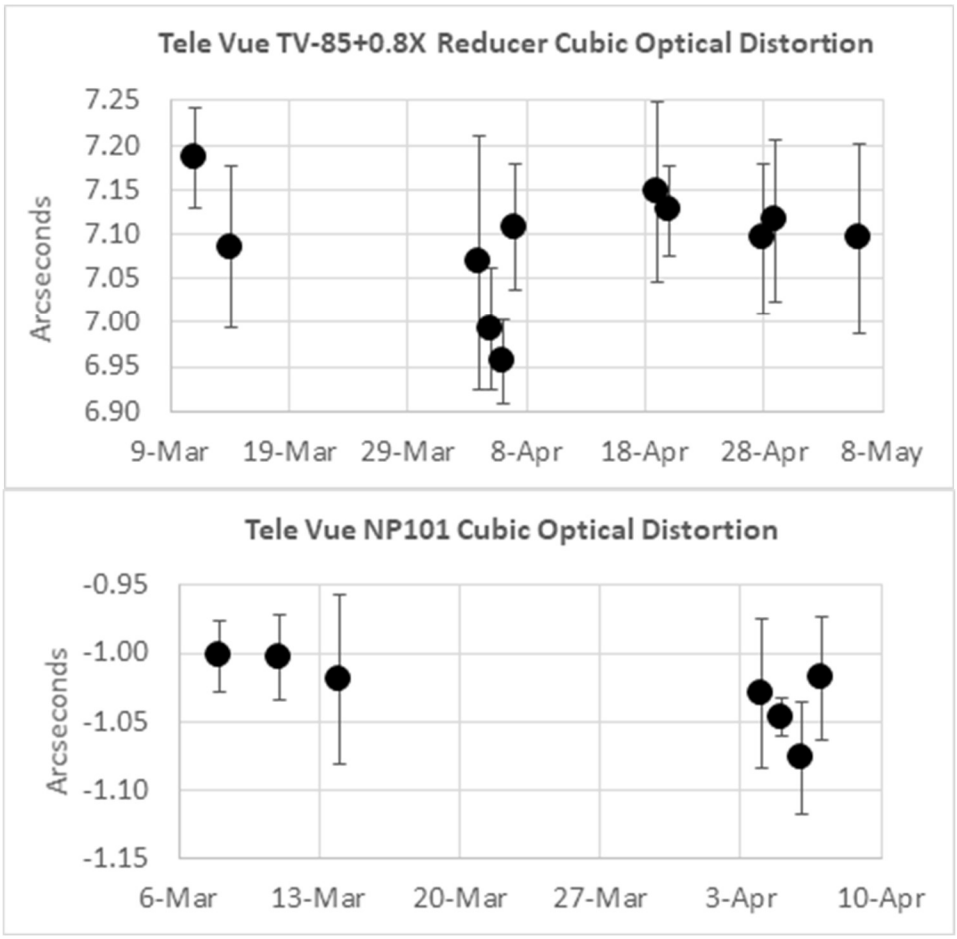

Figure 16. Mean cubic optical distortions for two telescopes, with error bars calculated based on the standard deviation over each night. The plotted values refer to a point on the X-axis at 95% of the maximum width, not at the image edges.

Optimized imaging configuration:

In the previous MEE expeditions, the Sun was usually placed near the center of the image. Upon further review, this wastes much of the camera sensor. Stars near the image center are not detectable, but that is where the cubic optical distortions are the smallest. Stars toward the edges of the field have the smallest deflections and the largest distortions. Distortion shifts orthogonal to the deflection shifts can be ignored. This is something to take advantage of if the maximum usable area is to be optimized.

Based on this geometry, the useful area of different telescopes, reducers, and cameras can be calculated. Two scenarios were calculated. For one case, when the cubic optical distortion component exceeded the gravitational deflection magnitude, that part of the image was rejected. Thus, if the cubic optical distortion coefficient was measured with 1% accuracy, every star position in the selected part of the image would be accurate to better than 1%. If the distortion was measured to be 1 arcsec, a 1% accuracy means the distortion was measured with

an uncertainty of 0.01 arcsec. The goal is to get the uncertainties somewhat less than the expected deflections. The second scenario was when the cubic optical distortion component exceeded three times the deflection magnitude, then only that part of the image was rejected. In that case, the measurement of every star position would be accurate to better than 3%. The stars inward from these boundaries have negligible cubic optical distortions. The numbers were converted to area in square degrees, plotted in Figure 17. This is the usable area for one image with the Sun in one corner. The Askar FRA500 series telescopes (paired with their reducer) have very small cubic distortions, so they have very large usable sky areas. Since most of the image will be far from the Sun in one corner, this means many more measurable stars will appear in the final data, reducing the data uncertainties.

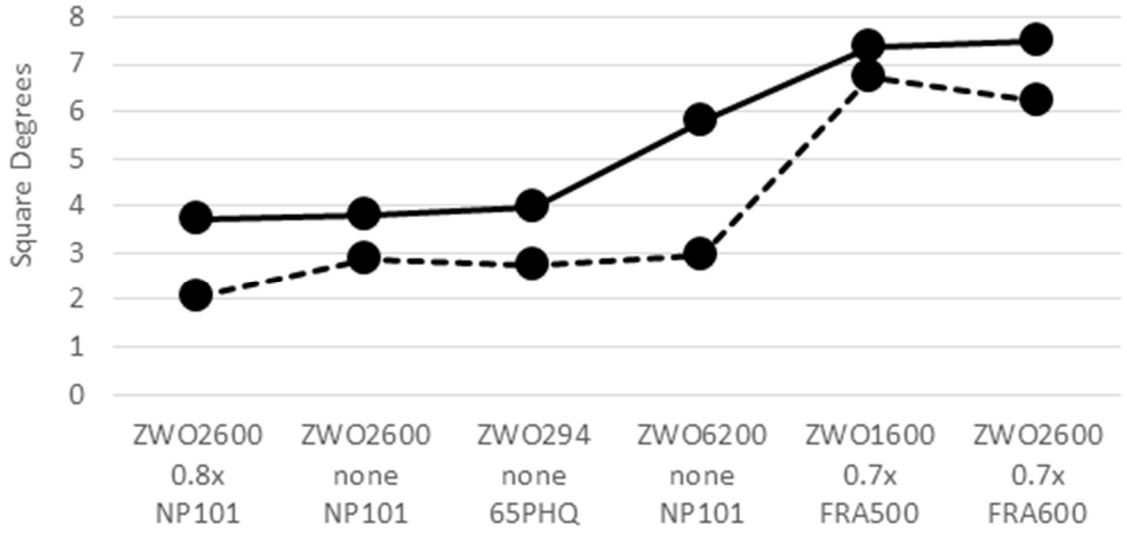

Figure 17. The usable sky area for some telescope and camera combinations is plotted in square degrees. The maximum ratio of the cubic optical distortion C divided by the gravitational deflection D, measured near the image edge, is limited to either 1.0 (dotted curve) or 3.0 (solid curve). The configurations include the camera model, the focal reducer coefficient (if used), and the telescope model. The data for the FRA600 has not been verified, but was based on the same design as the FRA500 telescope. Other cameras are available with similar sensors from other manufacturers.

MEE2027 star field optimization:

The star field for the 2027 eclipse is shown in Figure 18. The Beehive cluster (M44) is in the field of view, which offers many bright stars at a large distance from the Sun. The field of view for one image using the Askar FRA500 (with 0.7× reducer) with a ZWO ASI1600MM camera is shown in the upper right corner. Making a mosaic by placing the Sun in each corner is the goal. Considering the time for the telescope mount to move to these four fields, as well as two calibration fields 10 degrees away, the optimum field exposures can be estimated. The two

calibration fields at the start and end of totality will each consume 30 seconds of totality, and the four fields with the Sun in the corners will be 60 seconds each. This allows 70 seconds for mount pointing and settling, given that the totality in Qena, Egypt lasts 370 seconds. Integrated exposures of 30 to 60 seconds is enough to significantly reduce daytime atmospheric turbulence, which is expected to be significant in that location.

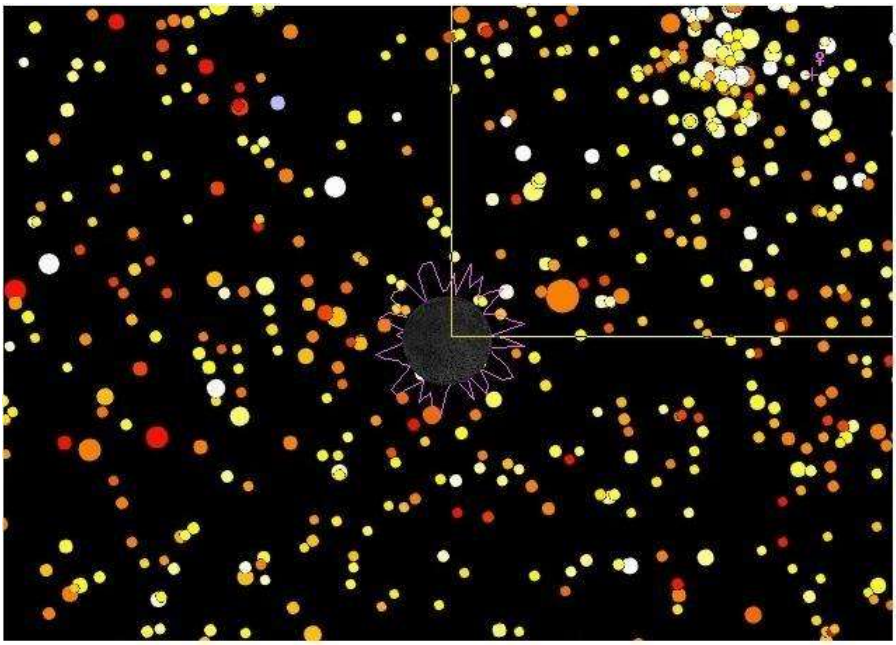

Figure 18. The star field for the 2027 eclipse is shown with stars down to magnitude 11. The colors are representative of the star spectral class. If a mosaic is made with the Sun in each of four corners, this optimizes the number of measurable stars. An Askar FRA500 telescope with a 0.7× reducer is used with a ZWO ASI1600MM camera in the outlined area.

Conclusions:

The MEE2024 eclipse research effort was successful. Most, but not all, of the goals were achieved. First was the use of modern CMOS cameras. Continuous imaging could take place since an exposure time of 100ms could be used for most of the cameras. This led to the acquisition of 7173 images during totality of 4.5 minutes. Using these short exposures allowed the opportunity to image stars close to the limb of the Sun.

Secondly, the number of stations was increased to 13, with a variety of telescopes and cameras. The variety of telescopes and cameras allowed for the evaluation of their optical performance. Prior to this analysis, the Tele Vue NP101is was thought to be the ideal telescope because it was known to have very low distortion coefficients. After evaluation, the Askar FR500 telescope (with reducer) may be the preferred telescope to use in MEE2027 because, surprisingly, it had virtually no distortion.

Next, was the fact that the three teams for the experiment contained students, faculty, and amateur astronomers from all over the world. All these team members are listed as authors on

the paper. The experience was very favorable for all, and the professional benefit to the undergraduate students involved in this challenging and high-quality STEM research experience cannot be underestimated. Already MEE2027 is attracting participants, including students and faculty from Portugal and Spain for a practice run during the 2026 eclipse. This eclipse is not particularly useful for accuracy, because it is very low to the horizon, but would serve well as an opportunity for student involvement and training for MEE2027.

The CMOS cameras all worked well. The ZWO ASI6200MM recorded more than 200 stars with a total of 480 usable frames with exposures of 250, 300 and 400 ms. The telescope on which the ZWO ASI6200MM camera was attached was not slewed away from the eclipse field of stars for calibration but nevertheless the data did allow the determination of the Einstein coefficient as 1.84 arcsec +/- 0.24 arcsec (within 5% of the accepted value of 1.75 arcsec). However, in the future, slewing to acquire calibration fields is highly recommended to decrease the uncertainty in deflection constant. The analysis of the cameras in MEE2024 led to the conclusion that the ZWO ASI2600MM is the desired camera for future use. This is based on a combination of sensor size, sensor technology, and image download speed. Also, the ZWO ASI1600MM is out of production.

As far as the locations for the execution of the MEE2024 are concerned, the three locations should have worked out well, but all were subject to an unusual occurrence of a tropical jet stream storm. It might have been a mistake to place so many telescopes in just three fairly closely spaced locations, in Mexico and Texas, all of which were subject to the same weather front. This area was chosen because of the length of the eclipse, altitude of the Sun and the probability of good weather. However, on the day, locations much further away, even in Vermont and Canada, had much more favorable conditions, despite on paper not being nearly so ideal. The lesson is that placing telescopes further apart along the eclipse path increases the chance for an organized effort to gather good data. For MEE2027, this might mean having telescopes placed along the coast of North Africa, as well as near the eclipse maximum in Egypt.

Perhaps the greatest success from MEE2024 may prove to be the creation of the open-source MEE Python data processing software. This allows processing of large data sets created by the CMOS cameras. It not only evaluates the errors created by the optics of the telescope but also finds centroids, stacks frames, then compares the centroids in the stacked images with the Gaia catalog for calculation of gravitational deflections. This program calculates the Einstein coefficient (including uncertainties) and displays these results in graphical form. This integrated piece of software, created by A. Smith (Cambridge University, England) and D. Smith (London, England) can be downloaded from GitHub (Smith & Smith, 2024). The MEE2024 data is posted on a tab at the website www.ModernEddingtonExperiment.org.

Finally, the last two goals of the MEE2024 experiment, getting very high accuracy results and imaging stars between one and two solar radii of the Sun's limb, were not realized. Our goal was to obtain an error less than 3% by collecting orders of magnitude more data than occurred in 2017. Unfortunately, bad weather prevented this. Similarly, no stars closer than 2.5 radii to the Sun were reliably imaged. Despite the failure of these two goals, we consider that the MEE2024 was very successful.

We are optimistic about the prospects for MEE2027. Plans are being made and participants are being recruited for the eclipse in Egypt in 2027 and the eclipse in Australia in 2028. Upon investigating all 50 total eclipses remaining in the 21st century, many of them were not suitable for the experiment. Fourteen eclipses are suitable for future experimenters. In order to assess the relative ability to obtain images in the inner corona, a close examination of the field of stars in these fourteen eclipses was performed. The results from this investigation are as follows.

Figure 19 shows the result of a simple sum of the deflections of all stars brighter than magnitude 9, with distance less than 2 solar radii, weighted by the sine of the angle above the horizon. This compensates for turbulence and uses only stars likely to be measured. Only eclipses with long durations over land are used. The red dots are for Egypt in 2027 and Australia in 2028. The number of measurable stars ranges from 1 (in 2024) to 4 (in 2027). Some eclipses have no measurable close stars.

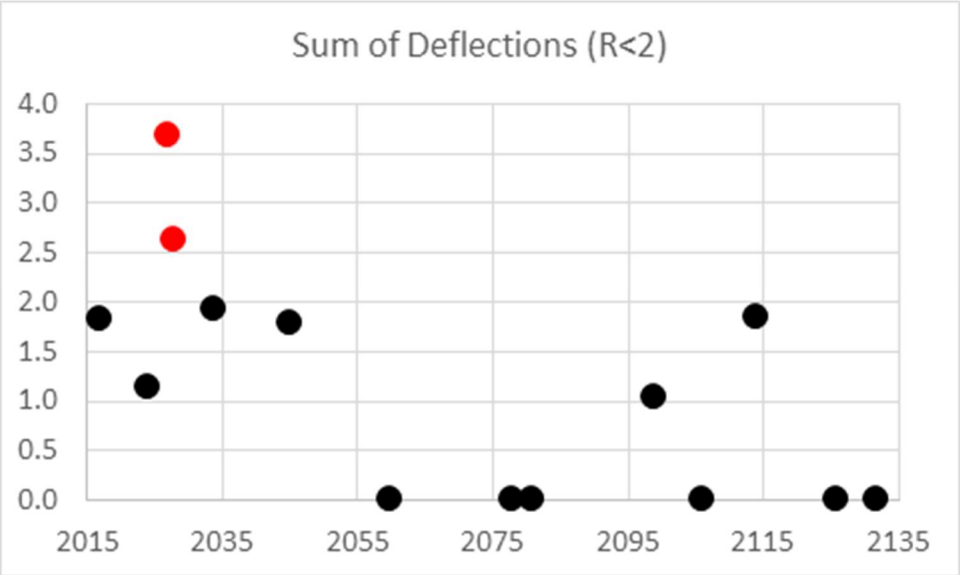

Figure 19: Future eclipses and their relative value in capturing stars closer than R = 2

Figure 20 is the quadratic sum of the deflections of all stars brighter than magnitude 9, with distance less than 2.5 solar radii, weighted by the ratio of the deflections compared to a standard star measured at R=2.5. This weighs the stars closest to the Sun, but includes more far from the Sun.

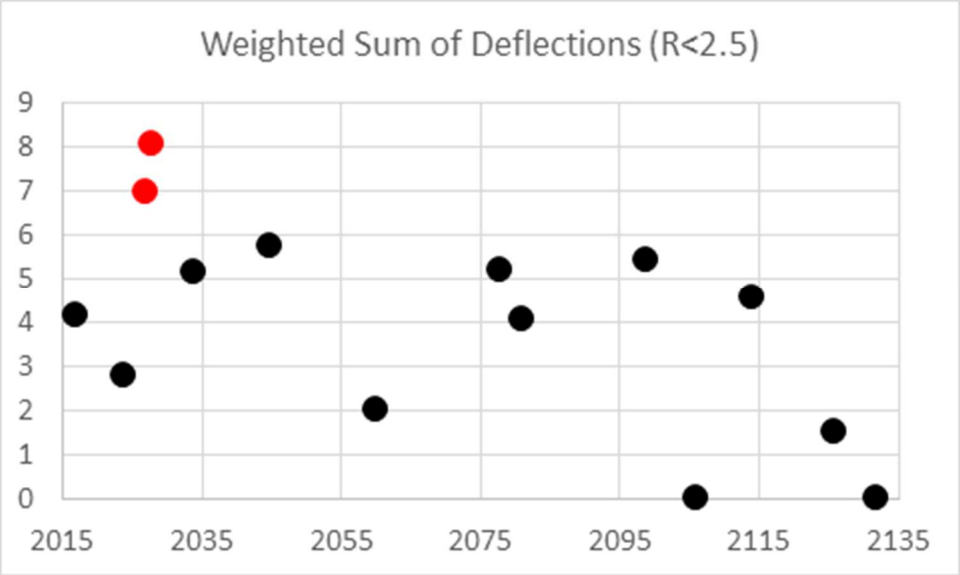

Figure 20: Future eclipses and their relative value in capturing stars closer than R = 2.5

Figures 19 and 20 demonstrate that the two eclipses in 2027 and 2028 are ideal for meeting the last goal of MEE2024 – creating a curve fit with data in the region R=1-2 solar radii. This would allow creation of a curve fit for the hyperbolic function which would be the first adequate verification of Einstein's General Relativity. The discussion above regarding the density and brightness of stars in the Forbidden Zone in the 2027 and 2028 eclipses makes it essential that MEE2027 and MEE2028 are successful in this regard. If these opportunities are not undertaken or the Forbidden Zone remains unimaged, the adequate verification may be postponed for another one hundred years since Einstein proposed the theory and Eddington first attempted to verify the theory. This puts great emphasis on the need for adequate funding and preparation for the next two performances of the Modern Eddington Experiment.

If you have interest in participation in MEE2027, would like to access the MEE2024 data at www.ModernEddingtonExperiment.org, or communicate with the authors, please email Toby Dittrich at tdittric@pcc.edu.

References:

Bertotti, B., Iess, L. & Tortora, P. A. (2003). A test of general relativity using radio links with the Cassini spacecraft. *Nature 425*, 374–376. https://doi.org/10.1038/nature01997

Brown, A. G. A., Vallenari, A., Prusti, T. J. D. B. J. H., De Bruijne, J. H. J., Babusiaux, C., Bailer-Jones, C. A. L., ... & Zwitter, T. (2018). Gaia Data Release 2 - Summary of the Contents and Survey properties. *Astronomy & Astrophysics, 616*, A1. https://doi.org/10.1051/0004-6361/201833051

Brune Jr, R. A., Cobb, C. L., DeWitt, B. S., DeWitt-Morette, C., Evans, D. S., Floyd, J. E.,

Lazenby, R. V., Marin, M., Matzner, R.A., Mikesell, A. H., Mikesell, M. R., Mitchell, R.I., Ryan, M. P., Smith, H. J., Sy, A., & Thompson, C. D. (1976). Gravitational deflection of light: solar eclipse of 30 June 1973 I. Description of procedures and final result. *Astronomical Journal, 81* (6), 452-454. https://doi.org/10.1086/111906

Bruns, D. G. (2018). Gravitational starlight deflection measurements during the 21 August 2017 total solar eclipse. *Classical and Quantum Gravity, 35* (7), 075009. https://doi.org/10.1088/1361-6382/aaaf2a

Campbell, W. W., & Curtis, H. D. (1914). The Lick Observatory-Crocker Eclipse Expedition to Brovarý, Russia. *Publications of the Astronomical Society of the Pacific, 26*(156), 225-237. https://doi.org/10.1086/122351

Campbell, W. W. (1923) The Total Eclipse of the Sun, September 21, 1922. *Publications of the Astronomical Society of the Pacific, 35*(203), 11-44. https://doi.org/10.1086/123262

Campbell W. W. & Trumpler, R. (1923) Observations on the Deflection of Light in Passing Through the Sun's Gravitational Field, Made During the Total Solar Eclipse of September 21, 1923. *Publications of the Astronomical Society of the Pacific, 35*(205), 158-163. https:doi.org/10.1088/123292a

Dittrich, W. A., Berry, R., Bruns, D., & Carrell, K. (2024). Modern Eddington Experiment 2024 (MEE2024). *Bulletin of the AAS, 56* (3). https://doi.org/10.3847/25c2cfeb.3ff37cfa

Dyson, F. W., Eddington, A. S., & Davidson, C. (1920). IX. A determination of the deflection of light by the Sun's gravitational field, from observations made at the total eclipse of May 29, 1919. *Philosophical Transactions of the Royal Society of London. Series A, 220* (571-581), 291-333. https://doi.org/10.1098/rsta.1920.0009

Earman, J. & Glymour, C. (1980) Relativity and Eclipses: The British Eclipse Expeditions of 1919 and Their Predecessors. *Historical Studies in the Physical Sciences, 11*(1): 49–85. https://doi.org/10.2307/27757471

Einstein, A. (1911). Über den Einfluß der Schwerkraft auf die Ausbreitung des Lichtes. *Annalen der Physik, 35*(10), 898-908. https://doi.org/10.1007/978-3-662-48039-7_8

Einstein, A. (1916). Die Grundlage der allgemeinen Relativitätstheorie. *Annalen der Physik, 49*, 769–822. https://doi.org/10.1002/andp.19163540702

Fomalont, E., Kopeikin, S., Lanyi, G. & Benson, J. (2009). Progress in Measurements of the Gravitational Bending of Radio Waves Using the VLBA, *The Astrophysical Journal 699*, 1395–1402. https://doi.org/10.1088/0004-637X/699/2/1395

Freundlich, E. F., & Ledermann, W. (1944). The problem of an accurate determination of the

relativistic light deflection. *Monthly Notices of the Royal Astronomical Society, 104* (1), 40-47. https://doi.org/10.1093/mnras/104.1.40

Froeschlé, M., Mignard, F. and Arenou, F. (1997) Determination of the PPN parameter γ with the
Hipparcos data. *Proceedings of the ESA Symposium `Hipparcos - Venice '97', 13-16 May, Venice, Italy, ESA SP-402*, 49-52

Gates Jr., S. J. & Pelletier, C. (2019) *Proving Einstein Right: The Daring Expeditions that Changed How We Look at the Universe.* PublicAffairs

Høg, E. ; Fabricius, C. ; Makarov, V. V. ; Urban, S., Corbin, T., Wycoff, G., Bastian, U., Schwekendiek, P., & Wicenec, A. (2000) The Tycho-2 catalogue of the 2.5 million brightest stars. *Astronomy & Astrophysics, 355*, L27-L31.

Kennefick, D. (2012). Not Only Because of Theory: Dyson, Eddington, and the Competing Myths of the 1919 Eclipse Expedition in Lehner, C., Renn, J., Schemmel, M. (eds.) *Einstein and the Changing Worldviews of Physics. Einstein Studies, Vol 12.* Birkhäuser. https://doi.org/10.1007/978-0-8176-4940-1_9

Kennefick, D. (2021). *No Shadow of a Doubt: The 1919 Eclipse That Confirmed Einstein's Theory of Relativity.* Princeton University Press.

Lebach, D. E., Corey, B. E., Shapiro, I. I., Ratner, M. I., Webber, J. C., Rogers, A. E. E., Davis, J. L. & Herring, T. A. (1995). Measurement of the Solar Gravitational Deflection of Radio Waves Using Very-Long-Baseline Interferometry. *Physical Review Letters, 75*, 1439–1442. https://doi.org/10.1103/PhysRevLett.75.1439

Mikhailov, A. A. (1959). The deflection of light by the gravitational field of the sun. *Monthly* Notices *of the Royal Astronomical Society, 119* (6), 593-608. https://doi.org/10.1093/mnras/119.6.593

Patel, K. (2024, April 3) A quest to prove Einstein right, beyond a shadow of doubt. *The Washington Post,* A3. Published online as Patel, K. (2024, April 8) 'Why this eclipse could really show Einstein was correct', *The Washington Post.* https://www.washingtonpost.com/weather/2024/04/08/eclipse-einstein-total-experiment-relativity/

Perrine, C. D. (1923). Contribution to the history of attempts to test the theory of relativity by means of astronomical observations. *Astronomische Nachrichten, 219*, 281-284. https://doi.org/10.1002/asna.19232191706

Price-Whelan, A. M., Sipőcz, B. M., Günther, H. M., Lim, P. L., Crawford, S. M., Conseil, S., ... &

AstroPy Coordination Committee. (2018). The AstroPy Project: Building an Open-science Project and Status of the v2. 0 Core Package. *The Astronomical Journal*, *156*(3), 123. https://doi.org/10.3847/1538-3881/aabc4f

Price-Whelan, A. M., Lim, P. L., Earl, N., Starkman, N., Bradley, L., Shupe, D. L., ... & AstroPy Project Contributors. (2022). The AstroPy Project: Sustaining and Growing a Community-oriented Open-source Project and the Latest Major Release (v5. 0) of the Core Package. *The Astrophysical Journal, 935*(2), 167. https://doi.org/10.3847/1538-4357/ac7c74

Prusti, T., De Bruijne, J. H. J., Brown, A. G., Vallenari, A., Babusiaux, C., Bailer-Jones, C. A. L., ... & Zschocke, S. (2016). The Gaia mission. *Astronomy & Astrophysics, 595*, A1. https://doi.org/10.1051/0004-6361/201629272

Reasenberg, R. D., Shapiro, I. I., MacNeil, P. E., Goldstein, R. B., Breidenthal, J. C., Brenkle, J. P., Cain, D. L., Kaufman, T. M., Komarek, T. A., & Zygielbaum, A. I. (1979) Viking relativity experiment: Verification of signal retardation by solar gravity. *Astrophysical Journal Letters, 234*, L219–L221. https://doi.org/10.1086/183144

Robitaille, T. P., Tollerud, E. J., Greenfield, P., Droettboom, M., Bray, E., Aldcroft, T., ... & Streicher, O. (2013). Astropy: A community Python package for Astronomy. *Astronomy & Astrophysics, 558*, A33. https://doi.org/10.1051/0004-6361/201322068

Schindler, S. (2013). Theory-laden experimentation. *Studies in History and Philosophy of Science Part A, 44*(1), 89–101. https://doi.org/10.1016/j.shpsa.2012.07.010

Shapiro, I.I. (1964). Fourth Test of General Relativity. *Physical Review Letters. 13*(26), 789–791. https://doi.org/10.1103/PhysRevLett.13.789

Smith, A. & Smith, D. (2024). *Modern Eddington Experiment codebase*. https://github.com/andrew551/MEE2024 and https://github.com/andrew551/MEE2024/releases

Tatum, J. (2024). 11: Photographic Astrometry in *Celestial Mechanics*. LibreTexts. https://phys.libretexts.org/Bookshelves/Astronomy__Cosmology/Celestial_Mechanics_(Tatum)/11%3A_Photographic_Astrometry

van Biesbroeck, G. (1953). The relativity shift at the 1952 February 25 eclipse of the Sun. *Astronomical Journal, 58*, 87-88. https://doi.org/10.1086/106825

von Klüber, H. (1960). The Determination of Einstein's Light-deflection in the Gravitational Field of the Sun. *Vistas in Astronomy, 3*, 47-77. https://doi.org/10.1016/0083-6656(60)90005-2

Will, C.M. (2014) The Confrontation between General Relativity and Experiment. *Living Reviews in Relativity, 17*, 4. https://doi.org/10.12942/lrr-2014-4

Will, C. M. (2015). The 1919 measurement of the deflection of light. *Classical and Quantum Gravity*, *32*(12), 124001. https://doi.org/10.1088/0264-9381/32/12/124001